New polarimetric and spectroscopic evidence of anomalous enrichment in spinel-bearing Calcium-Aluminium-rich Inclusions among L-type asteroids

M. Devogèle[1,2], P. Tanga[2], A. Cellino[3], Ph. Bendjoya[2], J.-P. Rivet[2], J. Surdej[1], D. Vernet[4], J. M. Sunshine[5], S. J. Bus[6], L. Abe[2], S. Bagnulo[7], G. Borisov[7,8], H. Campins[9], B. Carry[2,10], J. Licandro[11,12],W. McLean[7,13], N. Pinilla-Alonso[14]

[1]*Université de Liège, Space sciences, Technologies and Astrophysics Research (STAR) Institute, Allée du 6 Août 19c, Sart Tilman, 4000 Liège, Belgium*
[2]*Université Côte d'Azur, Observatoire de la Côte d'Azur, CNRS, Laboratoire Lagrange UMR7293, Nice, France*
[3]*INAF - Osservatorio Astrofisico di Torino, Pino Torinese, Italy*
[4]*Université Côte d'Azur, Obs. de la Côte d'Azur, UMR7293 CNRS Laboratoire Optique, Bv de l'Observatoire, CS 34229, 06304 Nice, France*
[5]*Department for Astronomy, University of Maryland, College Park, MD 20742-2421, USA*
[6]*Institute for Astronomy, 640 N. Aohoku Place, Hilo, HI 96720, United States*
[7]*Armagh Observatory and Planetarium, College Hill, Armagh BT61 9DG, UK*
[8]*Institute of Astronomy and NAO, 72 Tsarigradsko Chaussee Blvd., BG-1784 Sofia, Bulgaria*
[9]*Physics Department, University of Central Florida, P.O. Box 162385, Orlando, FL 32816-2385, USA*
[10]*IMCCE, Observatoire de Paris, PSL Research University, CNRS, Sorbonne Universités, UPMC Univ Paris 06, Univ. Lille, France*
[11]*Instituto de Astrofísica de Canarias (IAC), C/Vía Láctea sn, 38205 La Laguna, Spain*
[12]*Departamento de Astrofísica, Universidad de La Laguna, 38206 La Laguna, Tenerife, Spain*
[13]*Department of Physics, University of Warwick, Gibbet Hill Road, Coventry CV4 7AL, UK).*
[14]*Florida Space Institute, University of Central Florida, Orlando, FL 32816, USA*

Abstract

Asteroids can be classified into several groups based on their spectral reflectance. Among these groups, the one belonging to the L-class in the taxonomic classification based on visible and near-infrared spectra exhibit several peculiar properties. First, their near-infrared spectrum is characterized by a strong absorption band interpreted as the diagnostic of a high content of the FeO bearing spinel mineral. This mineral is one of the main constituents of Calcium-Aluminum-rich Inclusions (CAI) the oldest mineral compounds found in the solar system. In polarimetry, they possess an uncommonly large value of the inversion angle incompatible with all known asteroid belonging to other taxonomical classes. Asteroids found to possess such a high inversion angle are commonly called Barbarians based on the first asteroid on which this property was first identified, (234) Barbara. In this paper we present the results of an extensive campaign of polarimetric and spectroscopic observations of L-class objects. We have derived phase-polarization curves for a sample of 7 Barbarians, finding a variety of inversion angles ranging between 25 and 30°. Spectral reflectance data exhibit variations in terms of spectral slope and absorption features in the near-infrared. We analyzed these data using a Hapke model to obtain some inferences about the relative abundance of CAI and other mineral compounds. By combining spectroscopic and polarimetric results, we find evidence that the polarimetric inversion angle is directly correlated with the presence of CAI, and the peculiar polarimetric properties of Barbarians are primarily a consequence of their anomalous composition.

Keywords:
Asteroids, composition, Origin, Solar System, Polarimetry, Spectroscopy

1. Introduction

The first attempts to classify asteroids, mostly based on multi-color photometry and spectroscopy at visible wavelengths, led to the identification of the so-called S and C "complexes". Later on, taxonomy based on low-resolution spectra in the visible domain by Bus (1999), Xu et al. (1995), and Bus and Binzel (2002) (we will refer to it as SMASS taxonomy hereafter) resulted in the partition of the S-complex into several sub-classes, based on differences in spectral slope and drop of reflectance at wavelengths above 0.72-0.76 μm. Among them, the L-class includes asteroids having the smallest drop of reflectance and a relatively steep slope. The first goal of tax-

onomy is to differentiate asteroids based on their composition. However, the differences between the L and other classes (S, K, and A) identified using visible wavelengths data, are sometimes not very sharp and can lead to compositional misclassification. Another SMASS class, similar to the L, but exhibiting a slightly steeper spectral slope, was also introduced and named Ld (Bus and Binzel, 2002).

More recently, DeMeo et al. (2009) extended the SMASS taxonomy to the near-infrared region (from 0.82 to 2.45 μm), including the whole 1 μm silicate absorption band and extending up to the other major absorption band of silicates around 2 μm. Based on the observed behaviour in this larger wavelength range, most of the previously identified L-class asteroids

retained an L-classification. These asteroids were found to exhibit a strong absorption feature at wavelengths around 2 μm and an almost absence of the 1 μm band. However, several differences were also found with respect to the SMASS classification. Some objects previously classified as K- and A- were found to belong to the new L-class, whereas some SMASS L-class were moved to S-, D- or X-class in the new classification. The SMASS Ld-class was found to be almost fully contained in the new L- and D-class (DeMeo et al., 2009). For sake of clarity, in the rest of this paper any references to the SMASS taxonomy will be referred to as (SMASS), while the more recent DeMeo taxonomy will be referred to as (DM).

The degree of linear polarization of sunlight scattered by asteroid surfaces is a function of the phase angle, namely the angle between the directions asteroid-Sun and asteroid-observer. The resulting phase-polarization curves share common general morphology, with variations that are mostly albedo-dependent (for a recent analysis of the subject, see Cellino et al., 2015a, and references therein). The plane of linear polarization is almost always found to be either coincident with or perpendicular to the scattering plane (Dollfus et al., 1989; Muinonen et al., 2002). The state of linear polarization of asteroids is usually described using the P_r parameter, whose module is equal to the measured degree of linear polarization, but adding a sign, to indicate if the plane of polarization is found to be perpendicular (positive sign) or parallel (negative sign) to the scattering plane. Observations show that the range of phase angle for which P_r is negative extends from zero up to an *inversion angle* (α_{inv}) generally found around 20°. This region of the phase-polarization curve is commonly called the "negative polarization branch". At larger phase angles, the sign of P_r becomes positive ("positive polarization"). The details of the morphology of phase-polarization curves (the maximum value of negative polarization P_{min}, at which phase angle this is occurring $\alpha(P_{min})$, value of the inversion angle α_{inv} and slope of the curve around it) are not only diagnostic of the albedo (Cellino et al., 2015a), but have also been found to be useful to discriminate among different taxonomic classes based on reflectance spectra (Penttilä et al., 2005). Fig. 1 shows the typical asteroid phase-polarization curve of the asteroid (1) Ceres. The locations of P_{min}, $\alpha(P_{min})$, and α_{inv} are displayed and labelled.

Cellino et al. (2006) reported the discovery of the anomalous polarimetric properties exhibited by the asteroid (234) Barbara. The phase-polarization curve of this object possesses an unusually wide negative polarization branch, extending up to an inversion angle around 30°. Such behaviour had not been previously observed and was not predicted by theoretical models (Shkuratov et al., 1994). Because (234) Barbara had been classified as Ld in the SMASS taxonomy, other asteroids of this or similar taxonomic classes were subsequently observed and 18 objects sharing the same polarimetric behaviour of Barbara were found by Gil-Hutton et al. (2008), Masiero and Cellino (2009), Gil-Hutton and Cañada-Assandri (2011), Gil-Hutton et al. (2014), Cellino et al. (2014a), Bagnulo et al. (2015), and Devogèle et al. (2017a). They were collectively named *Barbarians* after the asteroid (234) Barbara. Barbarians are a class of rare objects which do not exhibit any
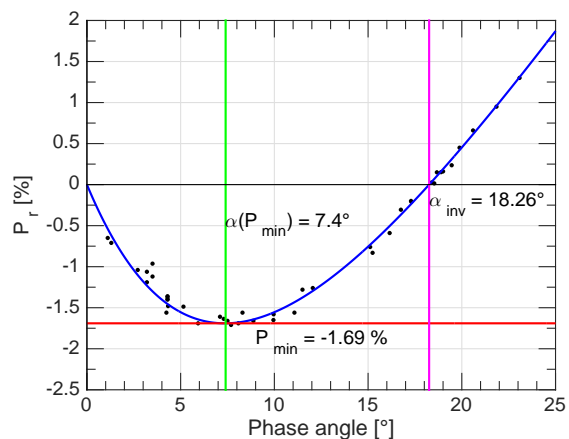

Figure 1: Example of the typical phase-polarization curve of (1) Ceres

preferred location within the asteroid main belt, apart from the presence of the Watsonia dynamical family (Cellino et al., 2014a), and possibly a few more, which members are Barbarians. In this paper, we will call "Barbarian" any asteroid exhibiting an inversion angle above 25°, independently on any other physical or dynamical property.

Tentative explanations have been proposed to explain the unusual polarimetric properties of the Barbarians. They include peculiar surface composition and/or texture properties, and/or the presence of large concavities that might introduce an unusual distribution of the directions of the incidence and emergence angles of scattered sunlight, with respect to the case of purely convex bodies. Barbara itself, in particular, has been extensively studied and was actually found to have a fairly irregular shape including large-scale concavities. The rotation period was also found to be unusually long ($P = 26.4744 \pm 0.0001$ h) (Tanga et al., 2015) compared to other asteroids of the same size. Other known Barbarian asteroids also exhibit slow rotation rates. In Devogèle et al. (2017b) we studied in more detail the role of possible concavities and also the significance of an anomalous abundance of slow rotators among Barbarians. However, it seems that we do not have enough evidence yet to draw any definitive conclusion.

Available reflectance spectra suggest that Barbarians have spinel-enriched surfaces. The first indication of this came from an analysis of the reflectance spectra of (387) Aquitania and (980) Anacostia performed by Burbine et al. (1992), well before the discovery of the Barbarian polarimetric properties of these two objects, by Gil-Hutton et al. (2008) and Masiero and Cellino (2009). Burbine et al. (1992) noted that these two asteroids, previously classified as S, show reflectance spectra clearly different from that of typical S-class asteroid. Both present a strong 2 μm absorption feature, and a nearly absent absorption feature around 1 μm while typical S-class spectrum is characterized by a 1 μm band stronger than the 2 μm one. These authors interpreted such behaviour as being due to the presence on the surface of unusually high amounts of the spinel mineral. Spinels ([Fe, Mg] Al$_2$O$_4$) are important components of the conglomerate of different element called Calcium

Aluminium-rich Inclusion (CAI) found in meteorites. Even a small fraction, typically from 10%-30%, of FeO enriched aluminous spinel ($MgAl_2O_4$) in CAIs can produce a strong absorption feature around 2 μm, similar to what we see in Barbarian spectra.

The CO chondrite meteorites exhibit the highest known abundance of CAI, but never exceeding 13% in volume. CV3 chondrites possess the greatest diversity of CAIs, but abundances are lower than 10%. Burbine et al. (1992) had originally suggested an abundance between 5 and 10% of CAIs on the surfaces of (387) Aquitania and (980) Anacostia considering an immature regolith. More recently, considering mature regolith, an analysis of the spectra of asteroids (234), (387) and (980) compared with laboratory spectra led Sunshine et al. (2007, 2008a) to conclude that a fraction of spinel-bearing CAIs of the order of ~ 30% in volume is needed to fit the observed near-infrared spectra of these asteroids. No known example of such high CAI abundances can be found in current meteorite collections. A high concentration of a particular type of CAI, called fluffy-type A, suggests a formation in an environment characterized by a high concentration of CAIs, and an absence of strong thermal alteration after formation.

FeO enriched aluminous spinel has a relatively high and variable real part of the refractive index in the visible part of the spectrum (Hosseini, 2008). It is found to be $n = 1.83$ in blue light, and decreases at longer wavelengths, down to $n = 1.78$ in the red and near-infrared (NIR), where it is almost constant. Sunshine et al. (2008b) suggested that a high refractive index might possibly be responsible for an uncommonly large inversion angle of polarization. In the case that a high abundance of spinel-bearing CAIs can be proven to be the correct explanation of the wide negative polarization branch observed for Barbarians, we would have good reasons to believe that these asteroids accreted in a nebula rich of refractory materials, and contain the most ancient mineral assemblage currently found in the inner solar system.

Based on the facts mentioned above, we started an observational campaign of L-class asteroids (both SMASS and DM) and known Barbarian asteroids. We present in Section 2 our new polarimetric observations done in the framework of Calern Asteroid Polarimetric Survey (CAPS) (Devogèle et al., 2017a) and at the Rozhen observatory as well as new spectroscopic observations carried out at the NASA Infra Red Telescope Facility (IRTF) using the near-infrared spectrograph SpeX (Rayner et al., 2003). The section 3 is devoted to the description of the models used to analyse the phase-polarization curve and the spectra of L-type asteroids. A Hapke model involving space weathering process is also described. In Section 4, the results relative to the spectral classification, the phase-polarization curve, the geometric albedo, the spectral fitting, asteroid families, and the identification of new Barbarians are presented. The Section 5 is devoted to the interpretation and discussion of the relation between (DM) L-type and the Barbarians, the composition of L-class asteroids, some interpretation for the high polarimetric inversion angle of the Barbarians. Finally, Section 6 presents our conclusions and perspectives for future works.

2. Observations

In this work, 36 targets were observed in polarimetry, spectroscopy or both. They were selected on the basis of satisfying one or more of the following criteria:

- Being a known Barbarian;

- Belonging to (SMASS) L- or Ld-class;

- Belonging to (DM) L-class;

- Being a member of one of the following dynamical families known or suspected to include Barbarians and/or L-class (SMASS or DM) members: Watsonia, Henan (Nesvorný et al., 2015) and, Tirela (Mothé-Diniz and Nesvorný, 2008), renamed Klumpkea by Milani et al. (2014).

2.1. Polarimetric observations

A high-priority goal of this work was to understand the reason of the abnormally large inversion angle of Barbarian. However, we included also some targets which were already known to be non-Barbarians. These targets belong to (SMASS) taxonomic classes which have been found in the past to include Barbarians. Their characterization allows us to better understand the relationship between spectroscopy and polarimetry.

The polarimetric data were acquired in two distinct observatories. Most of them were taken at the C2PU (Centre pédagogique Planète et Univers) facility of the Calern station of the Observatoire de la Côte d'Azur (Nice, France). The ToPol (Torino Polarimeter) was used to carry out the observations, that were part of the CAPS program started in early 2015. The ToPol is mounted on the Cassegrain focus (F/12.5) of the 1.04 m West telescope of the C2PU facility. It involves a Wedged-Double Wollaston prism, a configuration yielding the polarimetric reduced Stokes parameters q and u in one single exposure. All data were processed using classical aperture photometry, but using a curve of growth procedure (Bagnulo et al., 2011, 2015). This procedure consist of measuring the fluxes of the four replicas of the target using gradually increasing aperture size. The optimal aperture size is then selected by visual inspection of the values of q and u as a function of the aperture size. Full description of the instrument and the reduction techniques used for this instrument are described in Pernechele et al. (2012) and Devogèle et al. (2017a).

Some fainter targets were observed using the 2-Channel-Focal-Reducer Rozhen (FoReRo2) with a polarimetric mode retarder half-wave plate mounted at the 2 m telescope of the Bulgarian National Astronomical Observatory (Rozhen, Bulgaria). See Jockers et al. (2000) for a full description of the instrument. A single Wollaston prism is used to measure on each CCD acquisition either the q or u reduced Stokes parameter. A retarder wave-plate was recently added to more easily rotate the observed polarization angles. The retarder wave plate is not described in the original paper.

Table C.5 lists all the polarimetric observations presented in this paper. All the observations were done between December

20, 2014 and January 14, 2017. All measurements were done in the standard V Johnson-Cousins band.

2.2. Near-infrared spectroscopic observations

The new spectroscopic data presented in this work were obtained during two nights (September 21, 2014 and January 22, 2015). The asteroids were observed from 0.8 to 2.5 μm, using the SpeX instrument (Rayner et al., 2003) in the low resolution (R ∼ 200) PRISM mode mounted on the 3-meter NASA InfraRed Telescope Facility (IRTF) telescope on Mauna Kea. All the targets were observed near the meridian and solar analogue stars were observed near the target just after or before the target to calibrate out telluric absorptions and to correct for differences from the solar spectrum. A nodding procedure was used for each set of exposures. This procedure consists in acquiring a pair of spectra at two distinct locations on the CCD field (referred to A and B positions). A 0.8×15 arcseconds slit aligned north-south was used for all the observations. Flat field images were obtained by illuminating an integrating sphere. Spectra of an argon lamp were also taken immediately before or after the observation of the targets for wavelength calibration.

The extraction and first reduction of the spectra were carried out using the IRTF pipeline SpexTool (Cushing et al., 2004). This pipeline performs sky subtraction using the A-B pair, corrects for the flat field, calibrates the wavelength using spectra taken at the beginning and end of each target observation, and finally extracts the reduced spectra. The removal of telluric absorptions was performed using the ATmospheric TRAnsmission (ATRAN) model (Lord, 1992) on each individual spectrum. This correction constitutes a very important step since the water vapour has strong absorption bands around 1.4 and 2 μm.

The final spectrum of an asteroid is constructed by averaging all the individual observed spectra. A sigma clipping procedure is used to reject outliers that may occur due to cosmic rays contamination.

The new obtained NIR spectra were merged with SMASS visible spectra whenever available (see Sec. 3.2.1 for details on the merging procedure).

Table 1 summarizes all the spectroscopic observations presented in this work. For each target, the magnitude, number of AB pairs, total exposure time and airmass at mid observation are listed. The solar analogue star used for the reduction of each individual target is also listed so as its airmass at mid observation. All the reduced spectra, merged with the visible part when available, are displayed in Appendix A.

3. Data analysis

In this section, we present the data analysis tools that were used to interpret the polarimetric and the spectroscopic data.

3.1. Phase-polarization curve

As already discussed in Section 1, the phase-polarization curves exhibited by asteroids share a general morphology characterized by the presence of a so-called negative polarization branch, in which P_r has negative values. Negative polarization reaches an extreme value (conventionally called P_{min} in the literature) at a phase angle $\alpha(P_{min})$. For increasing phase angles P_r decreases in absolute value up to the inversion angle α_{min} around 20° for regular (non-Barbarian) asteroids, where it becomes null again. Beyond the inversion angle, P_r takes positive values and shows generally a linear increase up to the extreme values of phase angle that can be possible for asteroid orbits (see Fig. 1).

A frequently used model of the phase-polarization curve is the so-called "Exponential-Linear" model (Muinonen et al., 2009):

$$P_r(\alpha) = A \cdot [e^{(-\alpha/B)} - 1] + C \cdot \alpha \qquad (1)$$

where α is the phase angle, and A, B, and C are parameters to be derived by least-squares techniques. In a couple of recent papers (Cellino et al., 2015a, 2016a) the computation of the best-fit parameters for a large number of asteroids was carried out using a genetic algorithm. Having determined the values of A, B, and C, for any given object, the inversion angle was derived by some simple numerical method, while P_{min} and $\alpha(P_{min})$ were derived through a computation of the first derivative of Eq. 1 using the values of the parameters determined by means of the genetic algorithm.

In this paper, the strategy described by Cellino et al. (2015a, 2016a) is applied to a larger dataset which includes recent observations obtained at Calern and Rozhen. In addition, to increase the robustness of our results, we derived again the best-fit values of the unknown parameters in Eq.1 using another, independent approach. In particular, the inversion angle of the phase-polarization curve was analytically determined by evaluating

$$\alpha_0 = \frac{BCW\left(-\frac{A\exp\frac{-A}{BC}}{BC}\right) + A}{C} \qquad (2)$$

for values of phase angle different from 0, where W(x) is the positive branch of the Lambert function. An estimation of the 1σ uncertainty of the inversion angle computed in this way was obtained by using a Markov Chain Monte Carlo fitting procedure (MCMC). The estimation of the 1σ uncertainty was then done by fitting a normal distribution to the histogram of the derived α_0 values. The same procedure was used for the other parameters such as the degree of minimum polarization P_{min} and the phase angle at which it is occurring.

The results of the computations of polarimetric parameters based on the two independent approaches described above were found to be in excellent mutual agreement, the differences being found to be within the formal error bars computed by the two algorithms.

3.2. Spectral fitting

3.2.1. Visible-NIR spectral merging

In our analysis of the spectral reflectance properties, the first step was to merge together available spectra covering the visible and NIR regions. Note that we did not limit our analysis to the

	Asteroids					Solar Analogues	
Name	m_v	#AB pairs	$t_{\exp}$ [s]	Run	Airmass	Name	Airmass
(12) Victoria	11.9	5	200	2	1.30	SAO42382	1.86
(122) Gerda	13.9	5	900	2	1.31	BS4486	1.18
(172) Baucis	12.3	6	1080	1	1.48	SA 115-271	1.15
(458) Hercynia	13.0	8	960	1	1.22	SA 93-101	1.07
(611) Valeria	11.4	5	600	1	1.12	SA 93-101	1.42
(753) Tiflis	14.8	5	1000	2	1.05	Hyades 64	1.07
(1372) Haremari	14.6	7	1400	2	1.08	SA 98-978	1.10
(2354) Lavrov	15.8	6	1440	1	1.30	SA 115-271	1.15
(4917) Yurilvovia	16.2	8	1880	1	1.04	SA 115-271	1.06
(8250) Cornell	17.7	10	2400	2	1.14	Hyades 64	1.07
(15552) Sandashounkan	17.1	10	2400	1	1.05	SA 93-101	1.07
(19369) 1997 YO	15.9	10	2400	2	1.06	SA 102-1081	1.07
(26219) 1997 WO21	16.9	14	3360	2	1.26	SA 102-1081	1.07
(67255) 2000 ET109	16.5	10	2400	1	1.05	SA 115-271	1.06

Table 1: Observing conditions at the IRTF telescope. The first column corresponds to the number and the name of the observed asteroid, the second column gives the V magnitude of the target at the time of observation, #AB pairs stands for the number of AB pairs taken, $t_{\exp}$ is the total exposure time, the first run corresponds to the night of September 21, 2014 and the second run to the night of January 22, 2015, the Airmass columns give the airmass at mid-observation. The "Solar analogues" frame gives the solar analogue star used for calibration, and its airmass at mid-observation.

objects observed by us at IRTF, but also analysed L-type spectra taken from the literature. The major sources of visible spectra are the SMASS (Bus, 1999) and SMASS II (Bus and Binzel, 2002) data-bases, while for the NIR, most available spectra have been taken at IRTF in the framework of the MIT-UH-IRTF Joint Campaign for NEO Spectral Reconnaissance and also the new data presented in this paper. Merging visible and NIR spectra turned out to be a non-straightforward task. In particular, we found almost systematically noticeable differences in spectral slope between the red end of available visible spectra and the blue end of NIR data. This is not an unusual problem in asteroid spectroscopy. Moreover, the same object can sometimes exhibit bands that are visible in one spectrum, but not in others taken at different epochs. As an example of a difficult case, in the left part of Fig. 2 we show the case of the asteroid (234) Barbara which was observed both in SMASS and SMASS II as well as, previously, in the 8-colors Asteroid Surveys (ECAS, Zelner et al. (2009)). We can see that the red ends of the visible spectra are quite different. We can also notice that none of these spectra merge well with NIR data. However, the older ECAS data, which cover a wider range of NIR wavelengths, links very well to IRTF data from the MIT-UH-IRTF Joint Campaign and are compatible with SMASS I data in the blue part of the spectrum. In the case of asteroid (236) Honoria (see the right part of Fig. 2), SMASS II and ECAS data are available as well as two spectra in the near-infrared from SMASS IR (Burbine and Binzel, 2002) and IRTF (MIT-UH-IRTF Joint Campaign). One can see that in this case, the two NIR spectra show a more reasonable mutual agreement with each other and are also compatible with available ECAS data.

In general we find that the NIR spectra tend to show less variability than the visible spectra. In our procedure, we always multiply the NIR spectrum so as its blue-end merges with the red-end of the visible spectrum at the same wavelength (0.82 μm) simply removing visible data covering longer wave-

lengths. This is justified by the fact that the red end of visible spectra corresponds to a drop in sensitivity of the CCD detectors. However, different merging methods can lead to spectra showing different behaviour near the merging point. As a general rule, therefore, we base our assessment of the quality of the fit by looking at the morphology of the absorption features in the NIR region beyond merging wavelength. Especially, in some cases, an apparent absorption feature around 0.7-0.8 μm cannot be modelled by our procedure and is not taken into account.

3.2.2. Fitting techniques

The general approach we adopted to model the obtained spectra was to use a combination of a small number of candidate mineral components using a simplified Hapke spectral mixing model (Hapke, 1981, 1984, 1986). The idea is to linearly combine the spectrum of several candidate end-members to find satisfactory best-fits of the observed asteroid spectrum.

A technical problem with the adopted approach is that, working in terms of spectral reflectance (r), the spectra of intimately mixed materials do not combine linearly (Nash and Bowell, 1974). On the other hand, working in terms of single scattering albedo (w), the combination of different spectra is linear even when the materials are intimately mixed. The fitting procedure was then carried out in the following steps:

1. Convert spectral reflectance of the end-member spectra into single scattering albedo.
2. Combine linearly the single scattering albedo of the different end-members.
3. Convert back single scattering albedo into spectral reflectance.
4. Compare the combined reflectance spectrum with the spectrum of the asteroid to be fit.
5. Repeat the above steps using an optimization procedure until an acceptable fit is obtained.
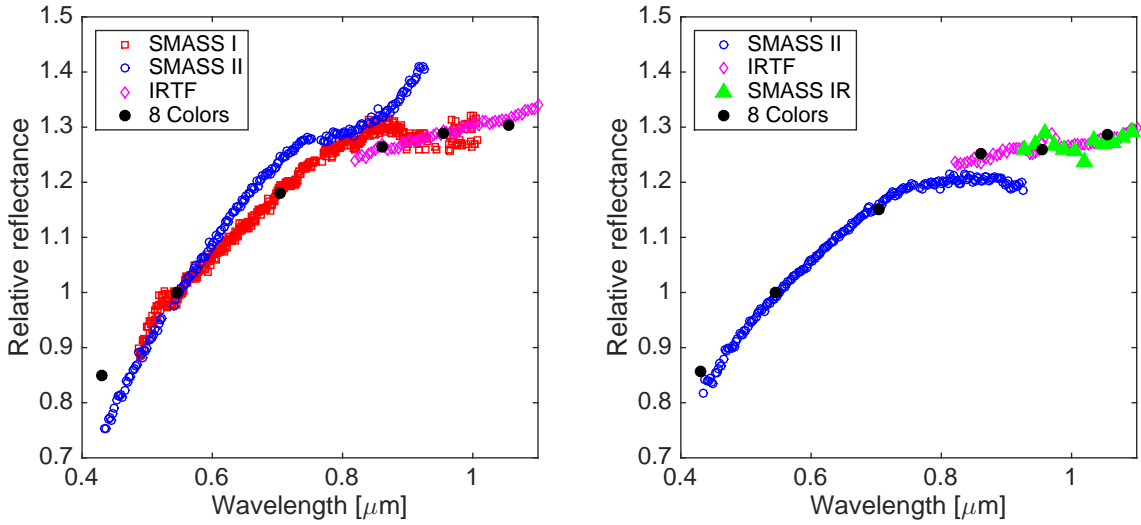
5

Figure 2: Example of Visible-Near-infrared merging issues for (234) Barbara (left part) and (236) Honoria (right part). SMASS I data are represented by red squares, SMASS II by blue circles, SMASS IR by green triangles, IRTF by purple diamonds, and ECAS data by black dots.

As the result of the fitting procedure, the relative abundance of each end-member in the obtained mixture is simply the coefficient used to linearly combine the single scattering albedo of the considered end-members.

The spectral reflectance of asteroid spectra is usually normalized to the value measured at the wavelength of 0.55 μm. The absolute reflectance could be therefore computed, in principle, by equalling the reflectance at 0.55 μm to the geometric albedo (p_V) of the object, when this is known. According to its definition, p_V is equal to the ratio between the object brightness measured at zero phase angle and that of an ideal, flat and perfectly Lambertian disk, having the same projected surface of the object, where the brightness is measured at the wavelength of 0.55 μm, and both the asteroid and the Lambertian disk are assumed to be located at unit distance from the Sun and from the observer.

However, the albedo of asteroid is usually known with a noticeable uncertainty. Most asteroid albedo come from the WISE (Masiero et al., 2011), NEOWISE (Mainzer et al., 2016), IRAS (Tedesco and Desert, 2002; Ryan and Woodward, 2010), and AKARI (Usui et al., 2012) surveys. Comparing the derived values of these surveys leads to differences as high as 20% and even more in many cases. Based on the difficulty in assigning a well determined value of geometric albedo to our objects, we allow it to vary in our optimization procedure.

Step (1) of the fitting procedure described above makes use of the equation linking the bidirectional reflectance r_c and the single scattering albedo w, according to (Hapke, 1981). This equation can be written as:

$$r_c = \frac{w}{4} \frac{1}{\mu_0 + \mu} \left[(1 + B(g)) P(g) + H(\gamma, \mu_0) H(\gamma, \mu) - 1 \right], \quad (3)$$

where μ_0 and μ are respectively the cosine of the incidence and emergence angles, g is the phase angle (*i.e.* the angle between the incident and reflected beams), and

$$\gamma = \sqrt{1 - w}. \quad (4)$$

Eq. 3 involves the three functions $B(g)$, $P(g)$ and $H(\gamma, x)$ which deserve some explanations. $B(g)$ is the backscatter function which defines the increase in brightness of a rough surface with decreasing phase. This effect is known as the opposition effect. According to Mustard and Pieters (1989) this function can be set to zero for phase angles greater than 15°. Since all the laboratory spectra used in this work were taken at a phase angle around 30°, $B(g)$ can be safely set to zero. $P(g)$ is the single particle phase function. Mustard and Pieters (1989) found that if one assumes an isotropic scattering (*i.e* putting $P(g)$ equal to one for all g), the resulting errors are of the order of a few percent. Since we do not know this function for all the end-members, we set $P(g)$ to one. $H(\gamma, x)$ is the so-called Chandrasekhar isotropic H function which can be approximated by the analytical expression:

$$H(\gamma, x) = \frac{1 + 2x}{1 + 2\gamma x} \quad (5)$$

where x represents μ or μ_0.

Laboratory spectra are normalized to a reference spectrum, taken at the same incidence and emergence angles, for which the single scattering albedo w can be assumed to be 1 (implying that all particle extinction is due to scattering). Eq. 3 can then be simplified and becomes (Hapke, 1993, 2001):

$$\Gamma(\gamma) = \frac{r_c(\text{sample})}{r_c(\text{standard})} = \frac{1 - \gamma^2}{(1 + 2\gamma\mu_0)(1 + 2\gamma\mu)}, \quad (6)$$

Eq. 6 can be solved for γ:

$$\gamma = \frac{\sqrt{\Gamma^2 \left(\mu^2 - \mu_0^2 \right)^2 + \Gamma (4\mu\mu_0 - 1) + 1} - \Gamma (\mu + \mu_0)}{4\mu\mu_0\Gamma + 1}. \quad (7)$$

From γ, the single scattering albedo for each end-member is then immediately derived (Eq. 4).

Once the single scattering albedo for each end-member has been combined linearly, the bidirectional reflectance of the mixture is computed back using the same equations to obtain the composite spectrum. The best abundance of each end-member which fits at best the asteroid spectrum is then derived using a Levenberg-Marquardt optimization technique.

3.2.3. Space weathering

Space weathering is a general process due to chemical and physical mechanisms that affect an airless body surface exposed to the space environment. It is the result of the exposure of an asteroid regolith to micro meteoritic impacts and heavy radiation (Solar wind and cosmic rays). It was observed that space weathering affects different bodies in different ways. In general, the effects of space weathering on bright, silicate-rich, asteroids tends to increase their spectral slope (reddening of the spectra), reduce the optical geometric albedo (darkening) and decrease the absorption bands depth (Chapman, 1996; Hapke, 2001; Brunetto and Strazzulla, 2013; Brunetto et al., 2014). However, recent studies have shown that the effect of space weathering on dark asteroid surfaces in nearly opposite. The reflectance spectrum tends to become bluer and brighter than fresh materials (Lantz et al., 2017). It is believed that these effects are due to the progressive implantation of nanophase metallic iron particles (npFe^0) into regolith grains, as the effect of micrometeoritic impacts and solar wind sputtering.

Hapke (2001) proposed a model to take into account the optical constants of iron within the host material to modify a spectrum in the framework of his Hapke reflectance and scattering theory. This model is based on the idea of computing the absorption coefficient of the host material (laboratory spectra) (α_h) and of npFe^0 particles (α_{Fe}). The total absorption coefficient (α) of the space-weathered material is considered to be simply given by the sum of the two:

$$\alpha = \alpha_h + \alpha_{Fe}. \tag{8}$$

In this work, we made use of this model to modify the spectra of each of our chosen end-members, to make them more similar to what we expect to be the case of space-weathered material on the surfaces of celestial objects. The first step is the computation of the single scattering albedo of each end-member using the procedure already explained above. Then, α_h is determined as:

$$\alpha_h = \frac{1}{D} \ln \left[S_i + \frac{(1 - S_e)(1 - S_i)}{w - S_e} \right] \tag{9}$$

where D is the effective size of the particles in the media, n is the refractive index of the end member, and S_e is the Fresnel reflection coefficient of the particle surface averaged over all angles of incidence for light incident from outside the particle, while S_i is the same, but for light incident from inside the particle. They are given by:

$$S_e = \frac{(n - 1)^2}{(n + 1)} + 0.05 \tag{10}$$

and,

$$S_i = 1.014 - \frac{4}{n(n+1)^2}, \tag{11}$$

The above expressions are useful approximation of the true integral given by Hapke (1993). In the case of S_i, Hapke (1993) used 1 instead of 1.014. However, Lucey (1998) found that in the range of refractive indexes n = 1.5 to 2, Eq. 11 is a better approximation.

As for the contribution of npFe^0, we have the relation:

$$\alpha_{Fe} = \frac{36\pi}{\lambda} \phi z \tag{12}$$

where

$$z = \frac{n_h^3 n_{Fe} k_{Fe}}{\left(n_{Fe}^2 - k_{Fe}^2 + 2n_h^2 \right)^2 + (2n_{Fe}k_{Fe})^2} \tag{13}$$

and ϕ is the volume fraction of npFe^0 that are embedded in the host material. n and k are the refractive index and absorption coefficient, respectively, of the host material (h) (end-member) and of iron (Fe).

If the iron particles are uniformly distributed $\phi = \rho_{Fe} f / \rho_h$ where ρ_{Fe} and ρ_h are the solid density of iron in the host material and the solid density of the host material respectively. Finally, f is the bulk mass fraction of iron.

The last step is to compute the new bidirectional reflectance of the space-weathered material using the following relations:

$$\Theta = \exp(-\alpha D) \tag{14}$$

and

$$w = S_e + (1 - S_e) \frac{1 - S_i}{1 - S_i\Theta} \Theta \tag{15}$$

from which, by using Eqs. 6 and 4, one can compute the final space-weathered spectrum. An example is shown, in the case of the fluffy type A CAI, in Fig. 3.

3.2.4. End-members

We describe here the end-members used in our analysis. All end-member spectra were obtained from the NASA REflectance experiment LABoratory (RELAB) spectral database.

In our case, the classical mixture of olivine and pyroxene, cannot be assumed. We have therefore to assume the presence, of spinel bearing CAIs (Burbine et al., 1992) like those found in CV3s meteorites to model the 2 μm band. Convincing arguments supporting this choice can be found in Burbine et al. (1992) and Sunshine et al. (2008a). A complete review of the mineralogy of CVs meteorite can be found in Cloutis et al. (2012).

We took into consideration different types of CAIs, that are known to produce large absorptions at wavelengths around 2 μm. In addition, we assumed the presence of the olivine mineral, one of the most important silicates found in many meteorites, as well as two example of the meteorites in which CAIs are found as inclusions. In particular, we chose the matrix of the well-known Allende and the Y-86751 meteorites. Note that we
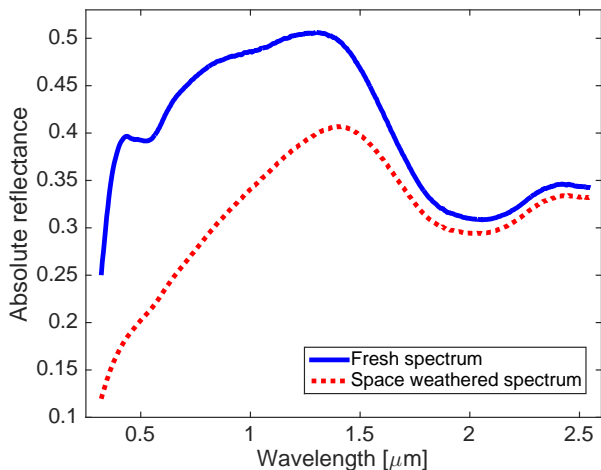
Figure 3: Example of the computation of the space weathering effect (see text) on the reflectance spectrum of the fluffy-type A CAI considered in our analysis.
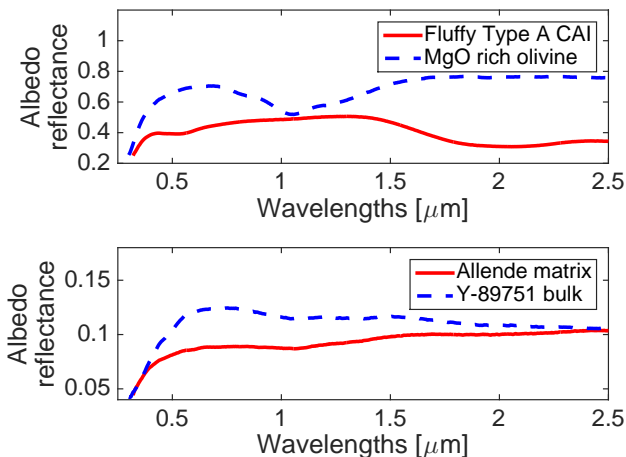

Figure 4: Spectra of all the end-members used to model the spectra of the asteroids studied in our analysis.

are aware that other possible materials could be taken into consideration. Moreover, we did some preliminary tests in which we included also pyroxene among the end-members, but these tests did not give satisfactory results. In what follows, we give a brief description of our selected end-members, while Fig. 4 shows the spectrum of each of them in terms of absolute reflectance.

Calcium Aluminium rich Inclusion - Three distinct types of CAIs (A, B and C) classified on the basis of petrography and geochemistry, are known to exist. The types B and C show evidence of melting by transient heating events before accretion. As opposite, fluffy type A CAIs (FTA) do not show any evidence of melting. FTAs are found in all chrondritic meteorites, whereas types B and C are found only in CV3 meteorites. FTAs and B type CAIs are both dominated by an absorption feature around 2 μm, but this absorption is much stronger in the case of FTAs. This stronger absorption feature is due to a much higher

concentration of FeO in the aluminous spinel present in these CAIs.

In this study we have considered the same spectra of CAIs, three FTAs and three B-type CAIs, already analyzed by Sunshine et al. (2008a) (RELAB: TM-TJM-001 to 005, and 007). The three FTA samples contain from 3 to 14% in weight mass of FeO while type B CAIs only a fraction of percent. The strength of the 2 μm absorption band is directly correlated to the abundance in FeO (Sunshine et al., 2008a). Considering that abundant FeO is excluded from CAI minerals during condensation, and that we see that CAI-types showing highest percentage of FeO also show an abundance of alteration phases, the FeO present in FTAs and B-type CAIs should come from post-accretion enrichment.

In our procedure, we always made use as end-member the FTAs sample showing the highest percentage of FeO. Type B CAI was always found to result in poorer fitting than using FTAs. This result was already noticed by (Sunshine et al., 2008a).

MgO rich olivine - Olivine is an important component of many meteorites, and is most abundant in chondrites. Differences in abundance and composition of olivines is an important criterion for the classification of meteorites (Mason et al., 1963).

Olivine is a magnesium-iron silicate. The most general formula is $\left[Mg^{+2}, Fe^{+2} \right] SiO_4$. The end-members are called forsterite (Fo) (Mg_2SiO_4) and fayalite (Fa) (Fe_2SiO_4). Olivine is usually described by the relative fraction of Fo and Fa (Fo_x and Fa_x). Forsterite is olivine with Fo_x between 100% and 90%, whereas fayalite is olivine with Fo_x between 0% and 10%. The spectrum of olivine shows a broad 1 μm absorption band which slightly depends upon Fo_x content.

The real part of the refractive index of olivine is highly dependent on the iron content. Lucey (1998) determined that the refractive index of olivine satisfies the relation $n = 1.827 - 0.192Fo_x$. This value of n appears to be constant over the whole interval of visible wavelengths.

Olivine is already present in the matrix of the meteoritic component that we are considering as end-members (see next paragraph). However, the composition of olivine is varying with respect to their degree of alteration. Unaltered olivine should be Mg-rich (forsterite) and the fraction of Fe will then increase as a function of the alteration. The olivine present in the considered meteoritic components possess moderate to large amount of Fe. On the other hand, some of our asteroids show less alteration than Allende or Y-86751 and should contain more MgO-rich olivine. As a consequence, we are considering forsterite olivine as end-member (RELAB: PO-CMP-076), which has a refractive index $n = 1.635$. The presence of forsterite in our model can then be seen as an indicator of post-accretion alteration.

CV3 meteorites - CAIs are one of the inclusions found in a matrix of material that constitutes the bulk composition of CV meteorites. The matrix must therefore be taken into account as one of the important constituents of any possible asteroidal composition.

In this work, we used two different CV3 meteorites. First,

we considered the matrix of the Allende meteorite from which CAI were removed (Sunshine et al., 2008a) (RELAB: MT-TJM-071). We also used spectral measurement of the Y-86751 meteorite (RELAB: MP-TXH-009).

The composition of the matrix of the Allende meteorite, the largest carbonaceous chondrite found on Earth, and one of the most studied examples of primitive meteorites, was measured by Bland et al. (2004). They found that it is composed of more than 80% of olivine. The Allende matrix is also found to be pyroxene-poor with only 5.9% of enstatite. The refractive index for the Allende matrix (after removing CAI inclusions) is unknown. Zubko et al. (2015) estimated a value between 1.68 to 1.83 for the Allende meteorite using the polarimetric inversion angle as a proxy. They found a value of 1.7 by fitting the light-scattering response from Allende meteorite particles. In this work we used $n = 1.7$ for the Allende matrix.

The Y-86751 meteorite is of the same type than Allende and possess the same bulk composition (Penttilä et al., 2005). Characterization using optical microscope to measure transmitted and reflected light shows flow texture possibly due to aqueous alteration (Gyo et al., 2011). It is known to contain CAIs where the spinel is more FeO-rich than Allende (18-25% (Murakani and Ikeda, 1994) instead of 4 to 14%). Its matrix also contain fine-grained aluminous spinel (Murakani and Ikeda, 1994).

3.2.5. Optimization procedure

The matlab *fmincon*[1] function was used as optimization procedure. This function allows the user to use constrained values of the optimized parameters. In our case, we set constraint on the end-member abundances so their sum will always be equal to 1.

Typical reduced chi-square optimization function was used. This function can be weighted in order to give priority to certain wavelengths. This is useful in the case of doubtful visible and NIR merging. In our case, only the near-infrared region, from to 0.82 to 2.5 μm, was considered to constrain the fitting procedure. This prevent the featureless visible part of the spectrum to play to significant role in case of plausible wrong visible and NIR merging.

4. Results

In this section we present the results of our analysis of polarimetric and spectroscopic data using the methods described in the previous Section.

Table 2 lists the 43 objects analysed in this work taking profit of the new spectroscopic and/or polarimetric data obtained in our observing campaigns. This table also summarizes some physical properties of the objects, and indicate family membership if any. Bold entries correspond to value directly determined in this work. Albedo values are taken from the NEOWISE (Wide-field Infrared Survey Explorer) catalogue

---

[1]More information about this function can be found on the Mathwork website: https://nl.mathworks.com/help/optim/ug/fmincon.html

---

(Mainzer et al., 2016), and can be affected by noticeable uncertainties, as suggested by Cellino et al. (2015a), and also by the fact that in some cases we have for the same object more than one albedo estimate, showing noticeable differences. This suggests that the nominal albedo uncertainties listed in the Table 2 can be in many cases fairly optimistic.

4.1. Spectroscopy

4.1.1. Spectral classification

Using IRTF, we have obtained new NIR spectra between 0.82 and 2.45 μm for 14 objects. For 9 of them, the visible part of the spectrum is available in the SMASS database and were merged together to produce the visible + NIR spectra. For each of them we derived a taxonomic classification according to the criteria used by DeMeo et al. (2009). Six objects are found to be (DM) L-class. The remaining three objects do not belong to the (DM) L class. (12) Victoria is a (DM) D-type, while (122) Gerda and (753) Tiflis are (DM) S-types. The information about the derived taxonomical classes of the asteroids observed in this work is included in Table 2 (bold entries). The other five observed asteroids for which no visible spectrum is available seem to be compatible with the (DM) L-class. However, no definitive classification can be made in the absence of the visible part of the spectrum.

4.1.2. Space weathering

Using space-weathered end-member spectra allowed us to model simultaneously the visible (even though the visible region is not taken into account in the optimization procedure) and near-infrared regions of the asteroid spectra. However, in applying our space weathering correction, some information about the optical properties of the end-members are needed. These properties are the real part of the refractive index n and the effective size of the end-members particles (D). We choose the values $n = 1.635$ for the Mg-rich olivine (Lucey, 1998), and $n = 1.7$ for the meteoritic component (see Section 3.2.4). In the case of the spinel bearing CAIs, we used the values computed of n with respect to wavelength derived by Hosseini (2008). However, Hosseini (2008) derived an n value valid only up to 1.4 μm, we considered n to be constant over a wider interval of wavelengths. According to (Gundlach and Blum, 2013) the average size of regolith particles may be dependent upon the size D of the asteroid, ranging from 10 to 100 μm for large asteroids (D >100 km) and from millimeter to centimeter for asteroids smaller than 100 km. However, the finest fraction of regolith particles is responsible for the principal optical effect of the space weathering (Pieter et al., 1993). We then choose the effective size of the particles to be equal to 25 μm. On the other hand, this model gives as a result the mass fraction of nanophase iron particle implanted on the regolith particles (see f column of Table 3). This parameter can be interpreted in terms of the extent at which an asteroid spectrum can be affected by space weathering. We show in Fig. 5 an example of the best fit obtained for asteroid (729) Watsonia when using fresh (left panel) and weathered (right panel) end-members.

Asteroid	Tholen	SMASS	DM	Barbarian	D (NEOWISE) [km]	p_V (NEOWISE)	Family
(12) Victoria	S	L	**D**	N	115.1 ± 1.2	0.16 ± 0.03	
(122) Gerda	ST	L	**S**	**N**	70.7 ± 0.9	0.25 ± 0.04	
(172) Baucis	S	L	**L**	Y	63.5 ± 3.1	0.13 ± 0.02	
(234) Barbara	S	Ld	L	Y	45.5 ± 0.2	0.20 ± 0.03	
(236) Honoria	S	L	L	Y	77.7 ± 1.2	0.16 ± 0.02	
(387) Aquitania	S	L	L	Y	97.3 ± 3.4	0.20 ± 0.03	
(402) Chloe	S	K	L	Y	55.4 ± 1.7	0.16 ± 0.03	
(458) Hercynia	S	L	**L**	Y	36.7 ± 0.4	0.43 ± 0.07	
(460) Scania		K	L		19.7 ± 0.1	0.26 ± 0.06	
(478) Tergestre	S	L		N	80.7 ± 1.0	0.17 ± 0.04	
(599) Luisa	S	K	L	Y	70.2 ± 0.5	0.12 ± 0.03	
(606) Brangane	TSD	K	L	**Y**	35.0 ± 0.2	0.10 ± 0.01	606
(611) Valeria	S	L	**L**	**Y**	57.5 ± 0.2	0.12 ± 0.01	
(642) Clara	S	L			38.2 ± 5.3	0.11 ± 0.02	
(679) Pax	I	K	L	Y	63.0 ± 0.4, 63.9 ± 0.2	0.11 ± 0.01, 0.10 ± 0.02	
(729) Watsonia	STGD	L	L	Y	50.0 ± 0.4	0.13 ± 0.01	729
(753) Tiflis	S	L	**S**	N	20.9 ± 0.8	0.33 ± 0.05	
(824) Anastasia	S	L	L	**Y**	32.5 ± 0.3	0.11 ± 0.03	
(908) Buda		L	D	**N**	30.8 ± 0.5	0.09 ± 0.01	
(980) Anacostia	SU	L	L	Y	74.7 ± 0.6	0.23 ± 0.06	
(1040) Klumpkea					22.3 ± 0.2	0.24 ± 0.04	1400
(1284) Latvia	T	L		**Y**	41.1 ± 0.5	0.08 ± 0.02	
(1372) Haremari		L	**L**	Y	26.5 ± 0.3	0.04 ± 0.01	729
(1406) Kommpa		Ld	D	**N**	24.2 ± 0.4	0.17 ± 0.05	
(1702) Kalahari	D	L			34.6 ± 0.1, 32.7 ± 0.2	0.06 ± 0.01, 0.06 ± 0.01	
(2085) Henan		L	L	**Y**	13.4 ± 0.1	0.30 ± 0.06	2085
(2354) Lavrov		L	**L**		13.3 ± 0.1	0.23 ± 0.05	2085
(2448) Sholokhov		L	L	**N**	38.5 ± 0.2	0.16 ± 0.02	
(2732) Witt		A	L		11.0 ± 0.3	0.30 ± 0.02	
(3269) Vibert Douglas					11.7 ± 0.2	0.14 ± 0.03	729
(4917) Yurilvovia		Ld	**L**		8.0 ± 2.4	0.21 ± 0.21	
(8250) Cornell					9.0 ± 0.3	0.34 ± 0.08	1400
(15552) Sandashounkan					7.6 ± 0.1	0.37 ± 0.04	1400
(19369) 1997 YO					14.3 ± 0.1, 13.6 ± 0.1	0.16 ± 0.03, 0.18 ± 0.02	1400
(26219) 1997 WO21					7.6 ± 0.2	0.22 ± 0.03	1400
(67255) 2000 ET109					6.6 ± 0.1	0.28 ± 0.02	1400
(673) Edda	S	S	L		37.6 ± 0.4	0.09 ± 0.03	
(3734) Waland		Ld	L		9.0 ± 0.2	0.20 ± 0.05	
(3844) Lujiaxi		L	L		15.0 ± 0.7	0.17 ± 0.03	2085
(4737) Kiladze		L	L		8.8 ± 0.1	0.15 ± 0.02	
(5840) Raybrown		Ld	L		9.7 ± 0.1	0.22 ± 0.04	
(7763) Crabeels		L	L		7.8 ± 0.1	0.22 ± 0.02	

Table 2: List of the targets observed (spectroscopy and/or polarimetry) during the different campaigns (upper part). Some targets which were not observed by us but discussed in this work were added in the lower part. Each bold entries mean that this is a result determined in this work. The first column corresponds to the number and name of the considered asteroid. The columns Tholen (Tholen, 1984), SMASS (Bus and Binzel, 2002; Mothé-Diniz and Nesvorný, 2008) and DM (DeMeo et al., 2009; Bus, 2009) stand for the taxonomic class in these 3 taxonomies. The Barbarian column indicates whether the asteroid is considered as a Barbarian (Cellino et al., 2006; Gil-Hutton et al., 2008; Masiero and Cellino, 2009). D (NEOWISE) and p_V (NEOWISE) correspond to respectively the diameter and the geometric albedo as given by the NEOWISE catalog (Mainzer et al., 2016). Finally, the Family column indicates the number of the parent member of the family in which the asteroid is classified (606 for the Brangane, 729 for the Watsonia, 1400 for the Tirela/Klumpkea and 2085 for the Henan family).
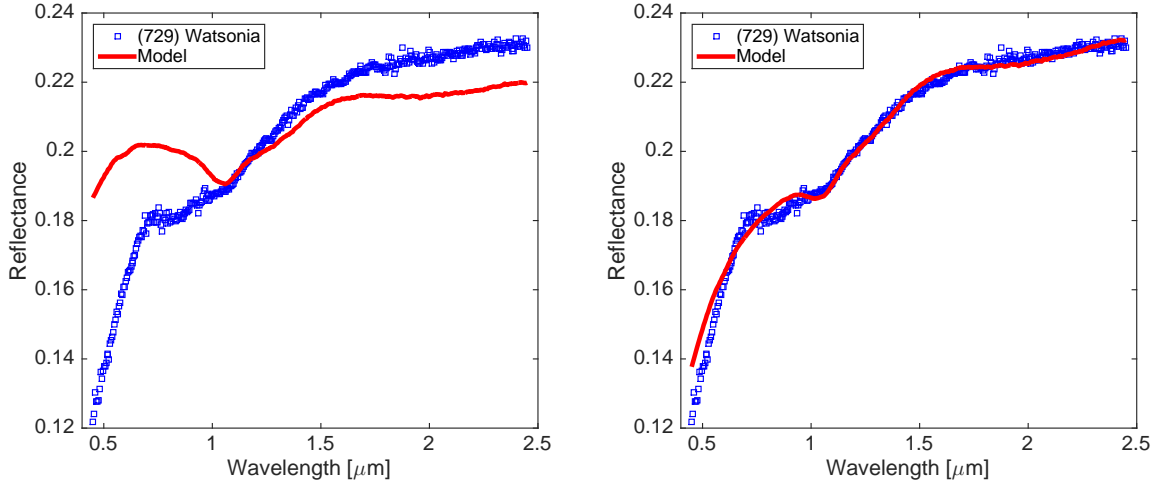
Figure 5: Example of the fits performed for asteroid (729) Watsonia using fresh end-members (left panel) and weathered end-members (right panel).

	Allende matrix						Y-86751 bulk					
Asteroid	FTA	Olivine	Allende	f	p_V	χ^2	FTA	Olivine	Y-86751	f	p_V	χ^2
(172) Baucis	29	32	39	0.078	0.15	2.96	17	29	53	0.115	0.13	2.45
(234) Barbara	25	62	13	0.039	0.24	3.26	20	65	15	0.047	0.24	3.05
(236) Honoria	12	29	58	0.061	0.09	3.82	0	51	49	0.093	0.15	3.79
(387) Aquitania	31	35	34	0.031	0.18	5.25	19	34	47	0.066	0.16	3.56
(402) Chloe	32	17	50	0.012	0.16	5.18	6	0	94	0.106	0.10	2.56
(458) Hercynia	32	14	53	0.019	0.13	3.29	9	1	90	0.121	0.09	1.86
(599) Luisa	24	29	47	0.074	0.15	3.29	8	30	61	0.121	0.13	2.32
(611) Valeria	3	11	85	0.085	0.19	1.60	0	68	32	0.080	0.08	3.09
(673) Edda	34	0	66	0.014	0.12	2.29	10	3	87	0.100	0.10	2.10
(679) Pax	26	20	53	0.036	0.14	4.12	0	0	100	0.186	0.08	1.24
(729) Watsonia	6	26	68	0.083	0.10	2.58	0	61	39	0.092	0.17	3.64
(824) Anastasia	45	9	46	0.000	0.19	9.33	10	0	90	0.030	0.12	4.82
(980) Anacostia	48	28	23	0.042	0.17	5.20	36	0	64	0.106	0.11	3.64
(1372) Haremari	13	56	31	0.085	0.12	2.44	0	44	56	0.137	0.12	1.85
(2085) Henan	36	6	58	0.000	0.13	1.88	10	0	90	0.075	0.10	1.49
(2354) Lavrov	41	35	25	0.028	0.18	1.47	26	20	54	0.065	0.14	1.35
(2732) Witt	27	56	17	0.045	0.22	2.47	22	58	20	0.058	0.21	2.17
(3734) Waland	40	16	44	0.017	0.15	1.75	17	0	83	0.088	0.10	1.50
(3844) Lujiaxi	51	12	37	0.000	0.19	1.78	28	0	72	0.031	0.13	1.32
(4737) Kiladze	49	0	51	0.020	0.14	2.46	29	0	71	0.073	0.12	1.92
(4917) Yurilvovia	20	45	35	0.061	0.15	8.10	5	32	62	0.140	0.11	6.05
(5840) Raybrown	39	30	31	0.010	0.18	3.82	22	0	78	0.075	0.10	3.04
(7763) Crabeels	49	11	39	0.022	0.18	1.16	32	0	68	0.071	0.13	1.09
(8250) Cornell	23	76	1	0.027		1.17	23	76	1	0.028		1.17
(15552) Sandashounkan	21	70	9	0.040		2.21	18	73	9	0.043		2.28
(19369) 1997 YO	8	0	92	0.103		1.13	2	67	31	0.079		1.96
(26219) 1997 WO21	18	77	5	0.017		1.06	19	77	5	0.019		1.07
(67255) 2000 ET109	22	45	33	0.062		1.51	13	57	30	0.075		1.69

Table 3: Result of the Hapke fitting procedure of reflectance spectra. For each object, identified by its asteroid number, we give the relative abundances of each of the three considered end-members in percent. The column (f) gives the fraction of npFe^0. The last column (Albedo) gives the reflectance at 0.55 μm of the fitted asteroid spectrum (no value when the visible part of the spectrum is missing).

4.1.3. Spectral fitting

The results of the spectral fitting procedure explained in section 3.2 are shown in Table 3. All fits are shown in Appendix B. The red continuous lines correspond to the results using the Allende matrix while the blue discontinuous lines are for the results obtained with the spectrum of the Y-86751 meteorite. For each fit, the plot of the residuals is shown below. In the majority of the cases, the residuals are smaller using Y-86751 than using the Allende matrix. All the spectra were normalized to unity at 0.55 μm, except those for which no visible counterpart was available. In those cases, the spectra were normalized to unity at 1 μm. For 3 of those, we have plotted the available Sloan Digital Sky Survey (SDSS) (Ivezić, 2002) measurements.

Sunshine et al. (2008a) modelled the spectra of (234) Barbara, (387) Aquitania, and (980) Anacostia using a slightly different approach. They found for these asteroids high CAI abundances never observed in meteorite samples, equal to 22%, 25% and 39% of spinel bearing CAIs, respectively. In their analysis, they used four different end-members. Fluffy type A CAI, CAI free Allende matrix, MgO rich olivine and the spectrum of (2448) Sholokhov to simulate the typical slope of a (DM) L-class asteroid. In our analysis, we find relatively similar values for the same three asteroids. Our values of CAIs abundances are respectively 25%, 31%, and 48%, when using the Allende matrix and 20%, 19%, and 36% using Y-86751.

As it was already mentioned in Sunshine et al. (2008a), only the fluffy type A CAI seems to be able to explain the observed spectra. Among the three different FTAs spectra adopted as possible end-members, the one showing the highest fraction of FeO ($\sim$ 14%) within spinel was always found to give a better fit. In no case, using B-type CAIs led to satisfactory fits of the spectra. We did some attempts to consider also pyroxene as a possible end-member (see Fig. 6). Even though in very few cases, very small amount of pyroxene (1% or below) could be added as a possible component, we found that pyroxene, in general terms, does not help to improve the fits of our spectra.

The composition of L-type asteroids seems to show some diversity as we observe different kind of behaviour. First, we notice that there are only two asteroids for which the Allende matrix provide a better fit (base on the χ^2). From these, (611) Valeria is the only one which is convincing. For the case of (729) Watsonia, the fit using the Allende matrix show a shallow absorption band around 2 μm which is not present in the asteroid spectrum. In the following, we will always discuss the result associated to Y-86751.

Only four spectra exhibit a positive slope from 1.5 to 2.5 μm (236, 611, 729, 1372). These spectra are also characterized by the total or nearly absence, of a 2 μm absorption band. As a result, our model does not need the addition of CAIs, but includes a large part of meteoritic component. Since the meteorite possesses by itself some CAIs, we can still consider that these asteroids are not CAIs free. We note that (729) and (1372) belong to the Watsonia family. Another member of the Watsonia family, (599) Luisa, also shows a low fraction of CAIs and shows a shallow absorption band around 2 μm associated with a null slope. We note that the visible part of the spectrum of (599) Luisa is not properly modelled.

Two asteroids possess very large amount of CAIs (> 30%). From those, the spectrum of (980) is relatively well fitted in both the visible and NIR regions. However, the fit could still be improved for the 2 μm absorption band which is shifted toward shorter wavelength in our modeling. The visible part of (7763) is not properly fitted, and also the fit of the 2 μm region is not ideal.

For four of them, the meteorite Y-86751 is almost the unique component (> 90%) associated with no (or almost no) olivine and a few percent of CAIs. These spectra are characterized by a monotonically decreasing slope after 2 μm, a high value of space weathering and low albedo. Two of them, (402) and (679), have a poor agreement in the visible region while the other two (458) and (2085) show a good agreement. Even though these asteroids do not show significant CAIs, their presence in the Y-86751 composition provides more or less 10% of CAIs. On the other hand, Y-86751 and Allende are almost absent for three asteroids (< 10%). All these three asteroids (8250), (15552), and (26219) belong the the Tirela family. The spectrum (only NIR) of these asteroids is well modelled with the highest fraction of olivine found in our sample and moderate fraction of CAIs.

The asteroid (824) Anastasia is a particular case. The model failed when using the Allende meteorite and produce a quite poor fit when using the Y-86751 bulk. The model provide 90% of meteoritic associated with 10% of CAIs. Although the fit is quite poor the Y-86751 bulk seems able to reproduce some very specific features such as a small absorption band around 1.1 μm. The spectrum of (824) Anastasia presents also a very steep slope in the visible which can be only very approximately reproduced. Although it seems that our model is missing some end-member to satisfactorily reproduce the spectrum of Anastasia, we also clearly see that the Y-86751 bulk seems to be the major component.

Our model failed in reproducing the spectrum of (2448) and (2732). The composition for these three asteroids should then be different than the rest of the L-class. In the case of (2448) this result agrees with the fact that this asteroid does not show a large inversion angle. We note that this asteroid was previously classified as A-type in the SMASS taxonomy.

4.2. Polarimetry

4.2.1. Phase-polarization curve

In this work, 109 polarimetric measurements of 32 individual asteroids are presented. All the observations were acquired using a standard Johnson V filter. The individual measurements P_r are listed in Appendix C.

Phase-polarization curves were built by using data from the literature to complement our new data. Literature data are available at the PDS web site[2], while others were taken from some recent papers (Gil-Hutton et al., 2014). The obtained phase-polarization curves were fitted using Eq. 1 whenever

---

[2]Planetary Data System. The data are available at the URL address http://pds.jpl.nasa.gov/ (files maintained by D.F. Lupishko and I.N. Belskaya)
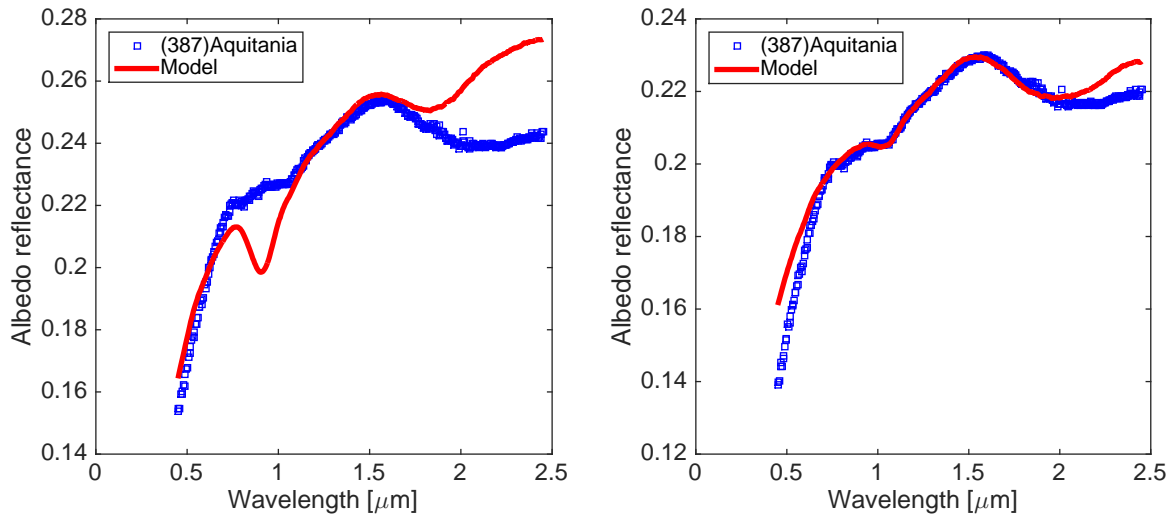
Figure 6: Best-fit models for the reflectance spectrum of asteroid (387) Aquitania. The left panel shows the best result obtained assuming the presence of pyroxene without CAIs. The right panel shows the opposite case, namely CAIs and no pyroxene.

enough data are available, using the techniques explained in Section 3.1.

Fig. 7 presents all the polarimetric measurements available for all asteroids studied in this work. In this figure and for all the following figures presenting polarimetric measurements, full symbols represent data obtained by us while empty symbols correspond to data retrieved in the literature. In Fig. 7, asteroids were subdivided into three groups based on their (DM) taxonomy. Those belonging to the (DM) L-class are plotted as black squares. Their phase-polarization curve is characterized by P_{min} around -1.5% occurring between 15 to 20 degrees of phase angle and an inversion angle between 25 to 30°. Asteroids which do not belong to the L-types are shown in blue circles. They display different phase-polarization curves which are not compatible with the one displayed by L-class. Those for which the (DM) classification is unknown are displayed as red diamonds. Some of these measurements are compatible with the phase-polarization curves of L-class objects, whereas others are not.

Among these 32 observed asteroids, 11 of them (172, 234, 236, 387, 402, 458, 599, 679, 729, 980, and 1372) were already known to be Barbarians (Cellino et al., 2006; Gil-Hutton et al., 2008; Masiero and Cellino, 2009; Gil-Hutton and Cañada-Assandri, 2011; Gil-Hutton et al., 2014; Bagnulo et al., 2015; Devogèle et al., 2017a). Our measurements allowed us to improve the coverage of the phase-polarization. For seven of them, the phase angle coverage is sufficient to calculate a phase-polarization curve. The measurements and derived phase-polarization curves for these asteroid are presented in Fig. 8. The derived polarimetric parameters are summarized in Table 4. From these, (172), (234), (236), (387), and (980) had been previously modelled (Gil-Hutton et al., 2008; Cellino et al., 2015a; Belskaya et al., 2017). Our results are in agreement with previously published phase-polarization modellings. The only major difference
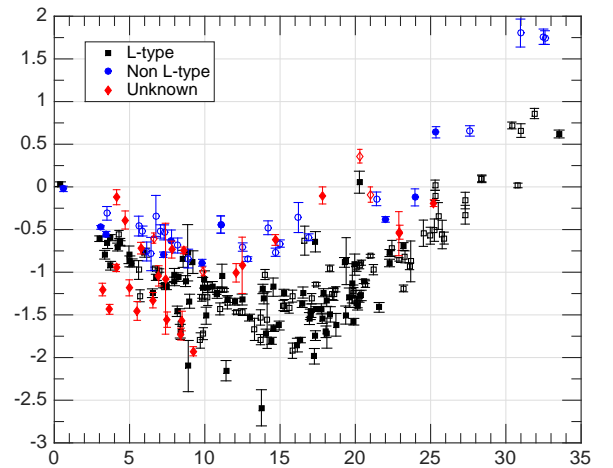
Figure 7: All polarimetric measurement of asteroids studied in this work. All full symbols correspond to data obtained by us while empty symbols correspond to measurements retrieved form literature. The black squares stand for (DM) L-type , the blue circles stand for asteroids which do not belong to the (DM) L-class, and the red diamonds stand for asteroids for which the (DM) classification is unknown.

13

Asteroid	α_{inv}	$\alpha(P_{\min})$	$P_{\min}$
(12) Victoria	23.0 ± 0.2	11.3 ± 0.1	-0.81 ± 0.01
(122) Gerda	18.4 ± 2.3	8.2 ± 0.5	-0.73 ± 0.05
(172) Baucis	28.1 ± 0.1	12.8 ± 0.2	-1.42 ± 0.02
(234) Barbara	29.4 ± 0.1	12.5 ± 0.4	-1.57 ± 0.04
(236) Honoria	26.6 ± 0.2	13.0 ± 0.1	-1.27 ± 0.01
(387) Aquitania	28.2 ± 0.5	13.7 ± 0.2	-1.46 ± 0.02
(402) Chloe	32.0 ± 0.4	15.7 ± 0.2	-1.68 ± 0.02
(679) Pax	28.2 ± 0.1	13.7 ± 0.1	-1.59 ± 0.02
(980) Anacostia	28.6 ± 0.5	12.5 ± 0.2	-1.24 ± 0.01
(1284) Latvia	26.1 ± 0.4		

Table 4: Summary of the phase-polarization curve parameters for some asteroids studied in this work. α_{inv} is the inversion angle, $\alpha(P_{\min})$ is the phase angle in the negative polarization branch where linear polarization reaches its largest (negative) value $P_{\min}$, which is listed in the last column.

concerns (234) Barbara for which the inversion angle is found to be 2° lower by Gil-Hutton et al. (2008) and Belskaya et al. (2017). This is mainly due to one measurement at $\alpha = 30.4°$ where $P_{\mathrm{r}} = 0.72$ (Gil-Hutton et al., 2008) which is not compatible with two more recent measurements at 30.8° and 33.54° which provide P_{r} equal to 0.017 ± 0.027 and 0.62 ± 0.046, respectively. More observations at high phase angle of (234) Barbara are needed to see if these contradictions between several observations are due to measurement errors or to intrinsic variation of the polarization degree measured in different observing circumstances.

For some targets, our measurements are the first polarimetric observations. The new data allow us, in some cases, to obtain for the first time an estimate of the inversion angle, leading us to decide whether they are Barbarians or not (we include this information in Table 2).

4.2.2. Identification of new Barbarians

The new polarimetric measurements presented in this work allow us to identify some new Barbarian asteroids.

(606) Brangane. For this asteroid, we have two polarimetric measurements at phase angles around 20°. The corresponding P_{r} values are around -1.2% which is a clear diagnostic of a Barbarian behaviour.

(611) Valeria. For this asteroid, we have two polarimetric measurements at similar phase angles around 20°. The corresponding P_{r} values are around -0.8% which is a clear diagnostic of a Barbarian behaviour.

(824) Anastasia. For this asteroid, we have five polarimetric measurements at phase angles ranging from 3.35° to 18.11° . The observed P_{r} values at $\alpha = 18.11°$ is $-1.71 \pm 0.18\%$ which is an indication of a Barbarian behaviour.

(1284) Latvia. Four polarimetric measurements are available at medium and high phase angles ($\alpha = 9.23°$, 22.89°, 22.95°, and 25.20°) with P_{r} values respectively equal to -1.93, -0.55, -0.53, and -0.19. The three measurements at phase angles higher than 22°, although one of them has a large error bar, nicely indicate an inversion angle around 26° which is clearly Barbarian-like.

(1372) Haremari. We have only one single measurement for this asteroid at a phase angle of 19.96° for which the value of P_{r} is $-0.911 \pm 0.124\%$. As for (606) Brangane, this negative value at a phase angle as high as 19.96° is by itself a strong evidence of its Barbarian nature. Haremari belongs to the dynamical family of Watsonia. This single available measurement for Haremari is in agreement with the (yet fairly noisy) phase-polarization curve of Watsonia, the largest remnant of this family. This is the first family identified among the Barbarians (Cellino et al., 2014a).

In addition to the above-mentioned objects, we have also one polarimetric observation of (2085) Henan, for which we find $P_{\mathrm{r}} = -1.920 \pm 0.090$ at a phase angle of 15.82°. This observation is still far from the inversion angle, but the polarization is strongly negative. This makes (2085) Henan a reasonable Barbarian candidate, to be confirmed by future measurements.

Fig. 9 shows the polarimetric data for the asteroids discussed in this Section. The phase - polarization curve of (234) Barbara is also shown for a comparison.

5. Discussions

5.1. The abundance of CAIs

In our sample of asteroids, we are observing a wide range of CAIs abundance from almost 0% (including the CAIs present inside the Y-86751 bulk) to more than 36%. This wide range of CAIs suggest that all the L-type asteroids do not have formed either in the same time and/or in the same location in the Solar nebula. This support the hypotheses that CAIs were spread inhomogeneously in the Solar nebula after their formation close to the Sun.

5.2. Relation between L-class (DM) and Barbarians

We already saw in Fig. 7 that L-class asteroids display a distinct phase-polarization characterized by the deep and very wide negative polarization branch typical of Barbarians.

The first Barbarian asteroids were discovered when asteroid taxonomy was based only on reflectance spectra limited to the visual region. We have already mentioned that, according to the SMASS taxonomy, these first Barbarians belonged to the L-, Ld- and K-classes. Later, it has been found that known Barbarians belong to the (DM) L taxonomic class, defined by taking into account also the NIR region of the spectrum.

Some asteroids belonging to the (SMASS) L-class have been included in our sample, even if there was no evidence that they belong to the (DM) L-class, to get a more definitive evidence that the Barbarian polarimetric behaviour is indeed uniquely associated with the (DM) L-class. These objects are (12) Victoria, (122) Gerda, (753) Tiflis. New spectroscopic measurements in the NIR presented in this work allow us to conclude that they belong to the (DM) D- (Victoria) and (DM) S-class (Gerda and Tiflis). Our polarimetric measurements for these three asteroids confirm that they do not exhibit a large inversion angle and certainly are not Barbarians (see Fig. 10).

Another asteroid in our sample, (908) Buda, was also classified as (SMASS) L-class, but it was later reclassified as a (DM)
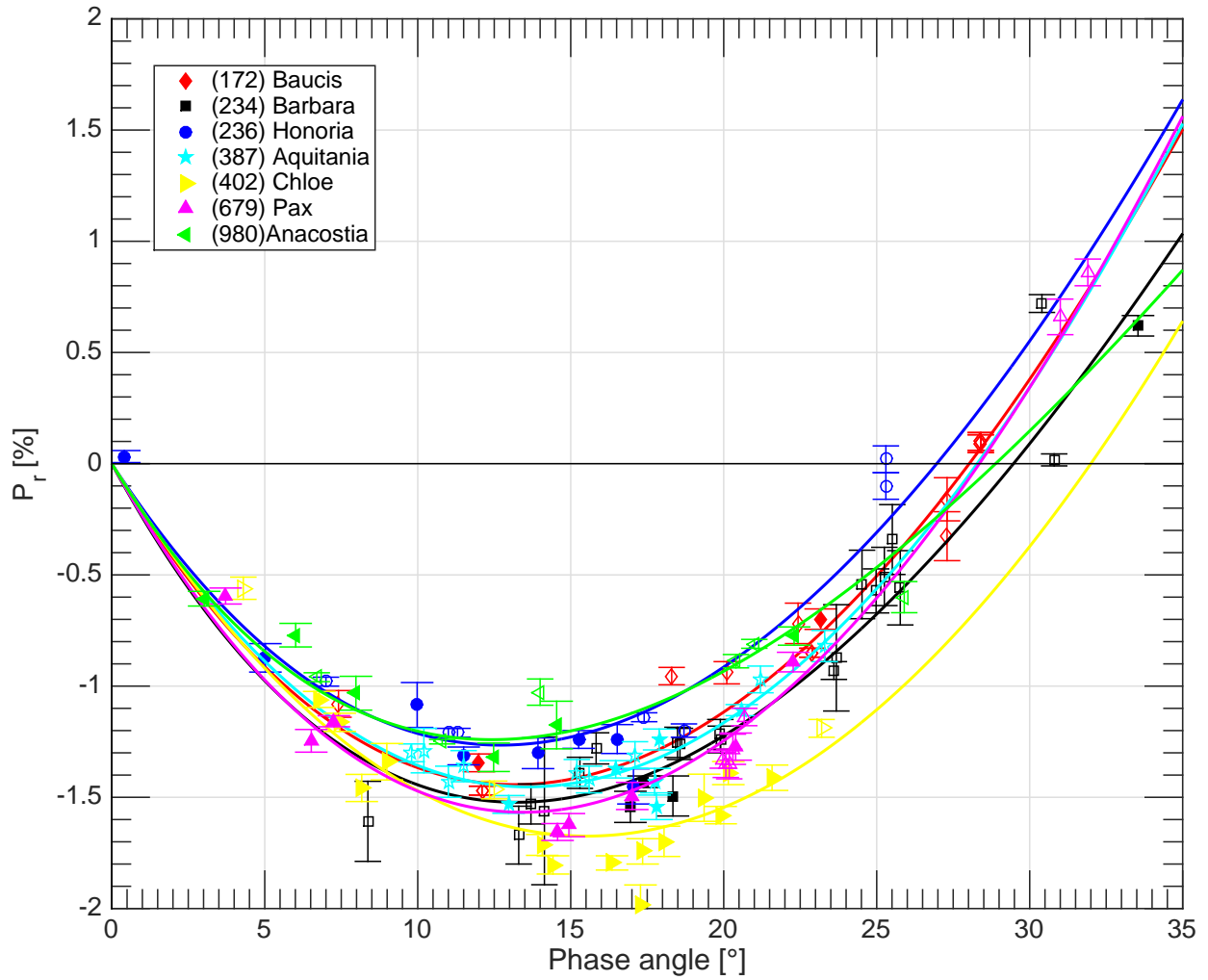
Figure 8: Phase-polarization curves derived for Barbarian asteroids using new polarimetric data presented in this work. These asteroids are the same as those of Fig. 11. Full symbols refer to data obtained in this work while open symbols refer to data obtained in the literature.
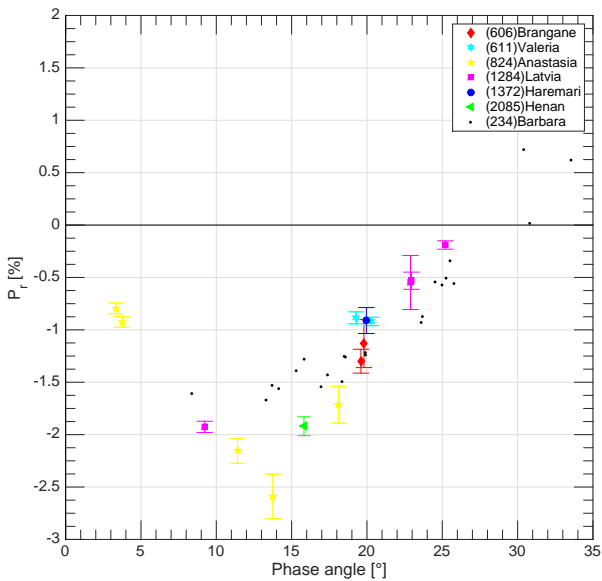
Figure 9: Polarimetric data for (606) Brangane (red diamonds), (824) Anastasia (yellow pentagrams), (1284) Latvia (magenta squares), (1372) Haremari (large blue disk), and (2085) Henan (green triangle). Polarimetric data of (234) Barbara are also shown as small black points for a comparison.
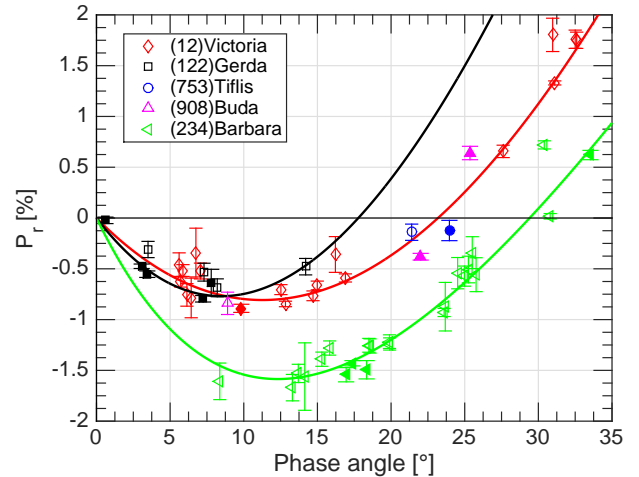

Figure 10: Polarimetric data for (12) Victoria (red diamonds), (122) Gerda (black squares), (753) Tiflis (blue circles), (908) Buda (magenta triangles), and (234) Barbara (green left-oriented triangles). The four first asteroids are (SMASS) L-type, but are not L-type in the (DM) taxonomy. (234) Barbara is an L-type in the (DM) taxonomy and a Barbarian. It is displayed here as reference for the typical behaviour of (DM) L-type /Barbarian asteroids.

D-class (DeMeo et al., 2009). Our two polarimetric observations of this asteroid at high phase angle ($P_r = -0.381 \pm 0.033$ at $\alpha = 22.01°$ and $P_r = 0.640 \pm 0.166$ at $\alpha = 25.36°$) suggest an inversion angle around 23°. This value is fairly high in general terms, but still too low to be considered as clearly diagnostic of a Barbarian asteroid, until new data will confirm or rule out this hypothesis.

Asteroid (1406) Komppa was already found to belong to the (DM) D-class (MIT-UH-IRTF survey), but it had been previously classified as a (SMASS) Ld asteroid. Our unique polarimetric measurements indicate a $P_r = -0.44 \pm 0.10$ at a phase angle of 11.06°. This phase angle is too low to draw any conclusion about its inversion angle, but the degree of linear polarization seems to be exceedingly low to be considered as a likely Barbarian candidate.

Some asteroids, (478) Tergestre and (1702) Kalahari are found to belong to the (SMASS) L-class, but no NIR spectra are available to determine the (DM) taxonomic classification. (478) Tergestre does not possess a large inversion angle and most probably is not a (DM) L-type asteroid. In the case of (1702) Kalahari, our polarimetric observations were taken at too low phase angles to draw any reliable conclusion.

On the other hand, asteroids (606), (824), (1372), and (with some more uncertainty) (2085), are found in this work to be Barbarians, and all of them are found to belong to the (DM) L-class. Based on these results, and on the fact that no Barbarian identified so far belongs to taxonomical classes other than the (DM) L-class, while only one peculiar (DM) L-class asteroid (2448) Sholokhov (see Sec. 4.1.3 for a discussion about this peculiar case), we can safely and definitively confirm the existence of a biunivocal relation.

5.3. Aqueous alteration

We found evidence in our modelling procedure that the meteoritic sample Y-89751 was almost always providing better result than using the matrix of Allende. As already discussed, these two meteorites are of similar type and similar bulk composition. Y-89751 contains CAI inclusions with more FeO-rich spinels (18-25% compared to 4-14% for Allende). Neither Allende nor Y-89751 present hydrated minerals on their matrices, but according to Gyo et al. (2011), the material in the groundmass around the chondrules of Y-89751 may show a flow texture due to aqueous alteration.

The possible presence of aqueous alteration for L-type asteroids was already suggested by Sunshine et al. (2008a) to explain the apparent absence of igneous differentiation that would have destroyed the observed FTAs (Grimm and McSween, 1989). On the other hand, Rivkin et al. (1998) observed a 3 μm feature on the spectrum of (387) Aquitania which is characteristic of aqueous alteration.

However, the improvement of the modelling with Y-89751 is not a proof of the presence of hydration on L-type asteroids. The improvement could as well be due to slight modifications in composition, FeO enrichment of the spinel and/or different preparation of the measured laboratory samples. Indeed, most of the differences observed between Allende and Y-89751 arise in the visible part of the spectrum and around the 2 μm absorption band. We do not see the typical 0.7 μm absorption feature associated to hydrated silicates neither in the spectrum of Y-89751 nor in that of Allende or any L-type studied in this work, and the 2 μm band is not diagnostic of aqueous alteration. Only a spectroscopic survey of L-types around 3 μm would assess the aqueous alteration of L-types.

5.4. Interpretation of the high polarimetric inversion angle of Barbarian asteroids

In this section, different possibilities are given to explain the large polarimetric inversion angle of Barbarian asteroids.

5.4.1. Regolith size

In a recent paper, Cellino et al. (2016a) have shown an updated version (see Fig. 9 of the above-mentioned paper) of a classical plot (see. for instance, Dollfus et al., 1989) showing the distribution of the asteroids in the space of the polarimetric parameters P_{min} versus inversion angle. The authors display that the Barbarians show a well distinct behaviour with respect to "regular" asteroids, since they occupy a region of the α_{inv} - P_{min} space corresponding to the domain occupied, according to laboratory experiments, by very finely divided silicaceous powders and thin lunar fines, whereas regular asteroids are usually found in a region of the plot corresponding to pulverized rocks and meteorites with coarser grains, having sizes between 30 μm and 300 μm. Cellino et al. (2016a) also noted that regular asteroids tend to group together, in the above-mentioned space, according to the albedo. In turn, the albedo is known to be a parameter that is related both to composition and regolith properties (see also, in this respect, Cellino et al., 2016b).

This polarimetric property suggests therefore that the Barbarian behaviour is related to anomalous surface regolith properties, in particular by regolith particle sizes much smaller than usual. Cellino et al. (2016a) also noted that another non-Barbarian asteroid, (21) Lutetia visited by the *Rosetta* probe, is also found in a location close to that occupied by Barbarians in the (α_{inv}, P_{min}) space. They noted that this asteroid is unusual in several respects, and there are reasons to believe that Lutetia is a primitive asteroid (Coradini et al., 2011; Sierks et al., 2011). The *Rosetta* instruments VIRTIS and MIRO also found evidence of very low thermal inertia (Gulkis et al., 2012; O'Rourke et al., 2012). This is in general agreement with polarimetric data suggesting that Lutetia's surface could be rich in fine dust.

Surfaces rich of fine dust could also be interpreted in terms of age, through the cumulative effect of a long exposure to moderate impacts unable to totally disrupt the body, but more than sufficient to finely pulverize its surface. This is a possible interpretation deserving further scrutiny, because we have already seen that the likely composition and also possibly the slow rotations of Barbarians could suggest that these asteroids could be extremely old.

However, the size of regolith is believed to be dependent on the asteroid size. The fact that Barbarian asteroids are also found among small members of dynamical family is contradictory with a relation between asteroid regolith size and Barbarian behaviour.

5.4.2. High abundance of spinel bearing-CAIs

Fig. 11 shows a graph of the relative abundance of fluffy type A CAIs (obtained by our analysis) against the inversion angle of the phase-polarization curve for some Barbarian asteroids for which we have decent phase-polarization curves. The asteroids
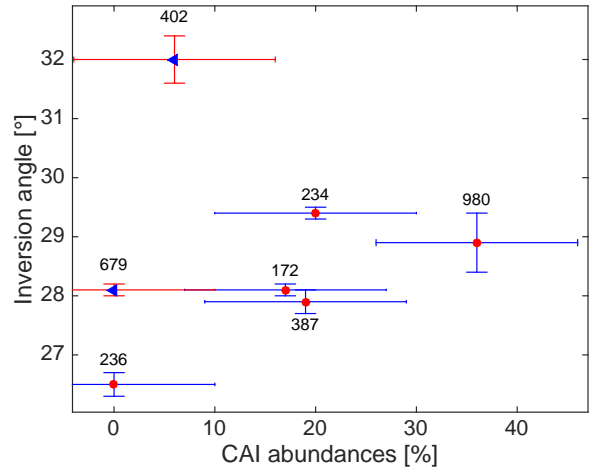

Figure 11: Plot of the polarimetric inversion angles for 7 Barbarian asteroids studied in this work, as a function of the derived CAI abundances obtained from fitting their reflectance spectra.

(402) and (679) have been represented using different symbol (blue triangles). Indeed, as already discussed in Sec. 3.2 these two objects seem to be different with respect to the other known Barbarians. Based on our model, they are the only ones (out of the 7) to be almost only composed of meteoritic component (100% for (679) and 96% for (402)). These asteroids also possess very high values of space weathering. We also note that the visible part of their spectrum is not well fitted in both cases.

With the exception of (402) and (679), a correlation between the modelled abundance of CAIs and the inversion angle seems to be apparent, in spite of the fairly large uncertainties in the determinations of CAI abundances. The interpretation of such a correlation is not trivial, however.

The results suggest that the polarimetric inversion angle of Barbarians tends to increase with increasing abundance of CAIs. According to current understanding, the only active phase of CAIs in determining the 2 μm absorption band in the reflectance spectrum is spinel. Moreover, there are reasons to believe that the strength of the absorption band is determined primarily by the spinel FeO content. So, when we plot our resulting abundances of the fluffy A-type CAI component in our modelled mineralogic compounds, we are also indirectly dealing with the FeO content of the spinel assumed to be present in the modelled CAI component.

One should note that even if (236) seems to not possess any CAIs, its spectrum is still modelled using meteoritic material which possess CAIs inclusions in which spinel has as much as 25% of FeO. Taking into account an abundance of CAIs of $\sim$ 10%, we can assume a CAI abundance of $\sim$ 5% for (236).

The most optically active compound inside CAIs is the FeO-bearing spinel. This material has a high refractive index which is highly dependent on the wavelength in the visible range (Hosseini, 2008). Because olivine, and also the meteoritic components (which are mainly composed of olivine) all have a refractive index mostly constant in the visible, an indirect proof for the presence of FeO-bearing spinel would be a wavelength

dependence of the polarimetric properties measured at different visible wavelengths (Zubko et al., 2015). Most polarimetric observations of asteroids have been historically done in *V*-band, only, but there are a few exceptions regarding asteroids particularly bright and/or interesting. Among them, there is (234) Barbara.

Fig. 12 shows our computations of the inversion angle of the asteroid (234) Barbara using data taken in the Johnson-Cousin *B*, *V*, *R* and *I* standard filters. In doing this plot, we are using some *BRI* data that are still unpublished and were obtained in the past mostly at the CASLEO observatory (San Juan, Argentina). In producing this plot, we chose to plot in the horizontal axis not the wavelength (which would be the direct observable, being based on the known properties of the standard photometric filters), but the value of the refractive index of spinel taken at the effective wavelength of each filter. As indication, the corresponding wavelengths are indicated in the upper horizontal axis. The value of the inversion angle is shown on the vertical axis. One can notice that, in spite of all uncertainties, there is a clear trend of increasing inversion angle with increasing refractive index. The error bars for the refractive index in Fig. 12 have been estimated based on the FWHM of each filters and the wavelength dependence of the refractive index. The errors are bigger at shorter wavelength since the refractive index is varying quickly in this region while it is almost constant for the I filter. One should take into account also that the sensitivity of most detectors decreases quickly in the blue spectral region, justifying the larger error bars for the inversion angle derived with the B filter. A similar variation of the inversion angle with respect to the wavelength was also found for the other Barbarian (599) Luisa. One spectropolarimetric measurement was acquired by Bagnulo et al. (2015) at high phase angle (26.9°). This measurement shows VRI polarization of respectively −0.39, −0.30, and −0.16%. This confirms the strong correlation of inversion angle with decreasing wavelength. However, in the case of Luisa, this variation is smaller. Based on our phase-polarization curve, Barbara would have VRI polarization of respectively −0.41, −0.18, and 0.15% at phase angle equal to 26.9°. One should note that the CAI abundance derived in this work for Luisa is mush lower than the one found for Barbara (8 and 20% respectively). This could be an explanation for the differences we observe between these two asteroids in spectropolarimetry.

The variations of the polarimetric inversion angle as a function of wavelength and of the derived abundance of CAIs suggest that the large inversion angles of Barbarian asteroids can be a consequence of a higher-than-normal and wavelength-dependent refraction index of the surface regolith, to be possibly interpreted as due to the presence of a high abundance of spinel-bearing minerals, fluffy A-type CAI being our preferred candidates to explain the available observational evidence.

5.4.3. Space weathering

Space weathering certainly affects the spectroscopic properties of the objects, but it is expected to affect also some polarimetric properties. The most direct effect of space weathering
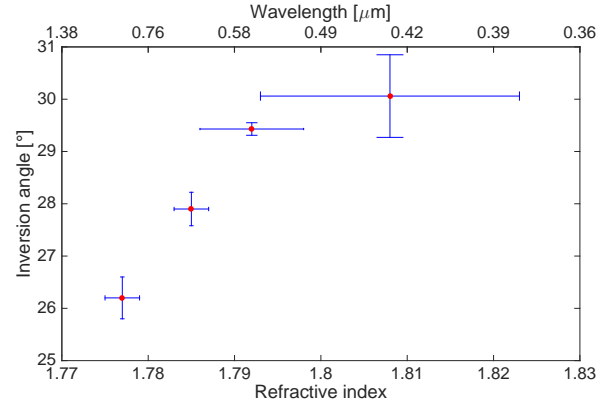

Figure 12: Inversion angle of (234) Barbara as a function of the refractive index of spinel and wavelength.
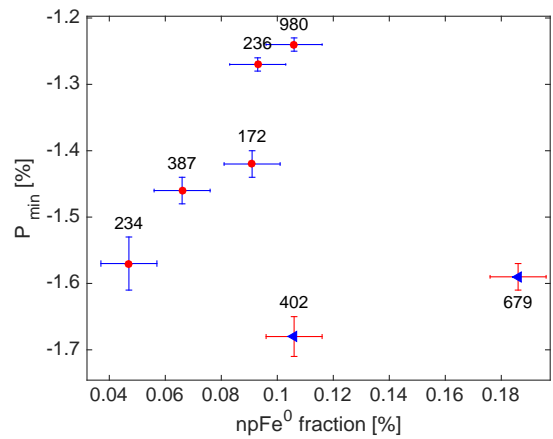

Figure 13: Abundance of npFe^0 (mass fraction) vs. P_{min}

(in the case of S-type asteroids) is a darkening of the surface and it is known that polarimetry is highly sensitive to the albedo.

Fig. 13 shows an apparent relation between the derived amount of nano-phase iron particles needed to fit the reflectance spectra, and the extreme value of negative polarization, P_{min}. This effect could possibly be interpreted as due to an increase of the imaginary part of the refractive index, according to Zubko et al. (2015). Since npFe^0 have a high imaginary refractive index, this interpretation is consistent with our results. As it was already noted for the relation between the inversion angle and the abundance of CAIs, the asteroids (402) and (679) seems (blue triangles) to follow a different behaviour.

5.5. Geometric albedos

Geometric albedos have been obtained for a large number of asteroids using the thermal radiometry technique applied to thermal IR data obtained by the WISE (Masiero et al., 2011) and AKARI (Usui et al., 2012) satellites. The results tend to suggest that (DM) L-class objects, including also the new ones identified in this paper, have an albedo which appears to be bimodal. The distribution is peaking around 0.11 and 0.18 as seen in Fig. 14.
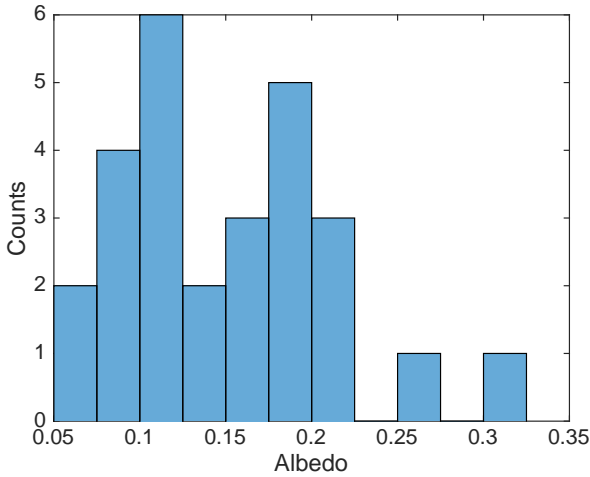
Figure 14: Histogram of the albedo of L type asteroids studied in this work.
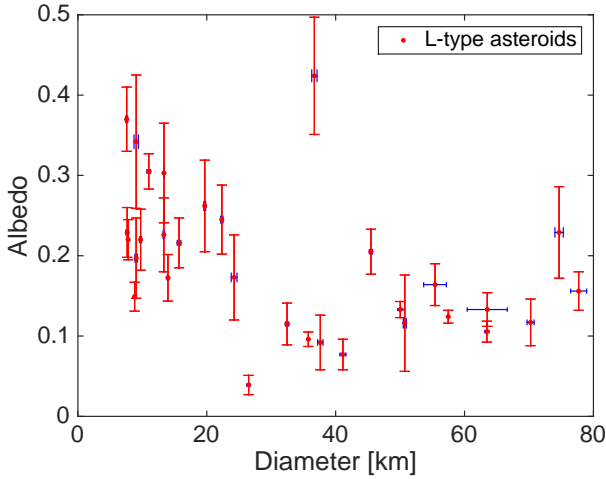

Figure 15: Albedo of (DM) L-type asteroids with respect to their derived IRAS diameter.

One should note that small L-type asteroids tend to have a higher albedo than bigger ones. Fig. 15 represents the albedo of L-type asteroids as a function of derived diameter by the NE-OWISE survey. Actually, all asteroids with a size below 20 km have an albedo higher than 0.15 while asteroids bigger than this treshold tend to have albedo lower than 0.15. This property is expected if space weathering act as a surface darkening process. Since the collisional lifetime decreases with the size of an asteroid (Farinella et al., 1992; Binzel et al., 2004), smaller asteroids are expected to have a younger surface than larger ones. This hypothesis was strengthened by the observation of a size dependence of the spectral slope of S-type asteroids (Gaffey et al., 1993; Carry et al., 2016). Binzel et al. (2004) also observed a correlation between the size and the spectral slope of near earth asteroids. Since the space weathering is also expected to increase the slope of asteroid spectra, a relation between size and slope, and albedo should also be expected.

Families supposed to be populated by (SMASS) L-type as-
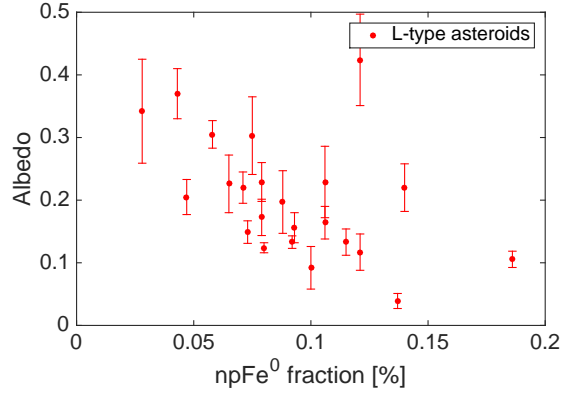
Figure 16: Abundance of $npFe^0$ (mass fraction) vs. the NEOWISE albedo for L-type asteroids.

teroids, such as the Henan (2085) and Tirela (1400) families, possess high albedos (respectively 0.22 ± 0.08 and 0.28 ± 0.11). However, only three of these asteroids were considered in the histogram presented in Fig. 14. It is then possible that more (DM) L-type high albedo asteroids will be identified in the near future.

The darkening property of space-weathering can be seen in our modelling. Fig. 16 shows the derived fraction of nanophase iron particle derived by our modelling procedure as a function of the NEOWISE albedo. This figure strongly suggests that the albedo decreases with the space-weathering in the case of L-type asteroids. However, according to Cellino et al. (2010) this property does not seem apply in the case of S-type asteroids.

5.6. Asteroid families

Asteroid families are groups of asteroids that share very similar orbital proper elements, and are interpreted as swarms of fragments issued from the disruption of single parent bodies.

The asteroids in our sample include some objects belonging to different dynamical families. Cellino et al. (2014a) identified for the first time the existence of an asteroid family composed of Barbarian asteroids, namely the Watsonia family. Two other families are suspected to include Barbarian asteroids, namely the families of Henan and Tirela/Klumpkea. Most members of these families are too faint to be observed by means of ToPol. However, we present here some polarimetric measurements and a few NIR spectra of candidate family members.

5.6.1. The Watsonia family

Asteroid (729) Watsonia was identified as the largest member of a dynamical family by Novaković et al. (2011). This is a high inclination family (proper inclination ~ 30°) located at an heliocentric distance of 2.76 AU. The parent member was found to be a Barbarian by Gil-Hutton et al. (2014). By means of VLT polarimetric observations of a sample of Watsonia family members, Cellino et al. (2014a) discovered the first known case of a family consisting of Barbarian asteroids.

The polarimetric measurements presented in this work of the parent body (729) Watsonia are shown in Fig.17, together with
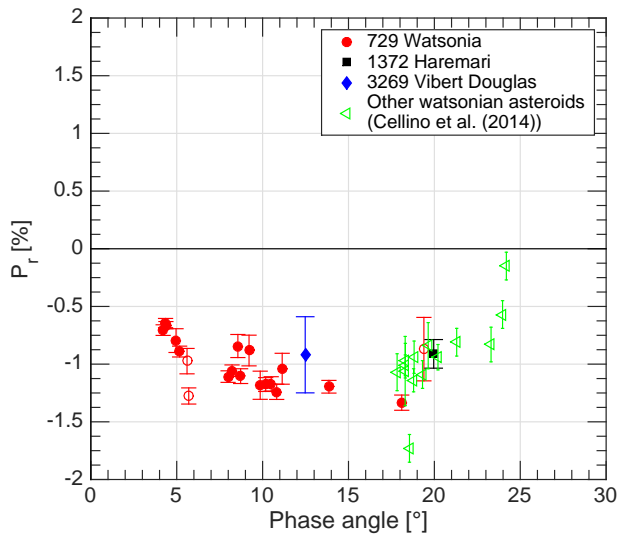
Figure 17: Polarimetric data of asteroids belonging to the Watsonia family

Figure 18: Spectra of (599) Luisa, (729) Watsonia, and (1372) Haremari normalized to one at 0.55 μm.

Figure 19: Spectra of (2085) Henan, (2354) Lavrov, and (3844) Lujiaxi normalized at 0.55 μm.

our measurement of the other largest asteroid in this family, (1372) Haremari, and (3269) Vibert-Douglas. Our data confirm that they seem to share the same polarimetric properties of Watsonia (see Fig.17). However, in the case of (3269) Vibert-Douglas the only one available measurement is insufficient to confirm a Barbarian behaviour.

The asteroid (599) Luisa can also be considered as a member of the Watsonia family (Cellino et al., 2015a). A more ancient super-family including also the nearby Barbarians (387) Aquitania and (980) Anacostia is also suspected to exist (Cellino et al., 2014a). Our polarimetric measurement of Luisa has been taken at a phase angle too low to conclude that Luisa is another confirmed Barbarian. However, Bagnulo et al. (2015) presented one spectropolarimetric measurement at high phase angle of this asteroid confirming its Barbarian nature. They exhibit similar spectra, (see Fig. 18), with relatively low CAI abundances (0% for (729) and (1372), and 8% for (599)). These results strengthen the hypothesis that these bodies are genetically related.

Figs. 17 and 18 show the available polarimetric and spectroscopic data, respectively, for asteroids belonging to the Watsonia family.

5.6.2. The Henan family

Brož et al. (2013) identified a family of 946 asteroids with (2085) Henan as the largest member, but Masiero et al. (2013) did not classify this as a family because it is too dispersed and probably contaminated by many interlopers. This controversial family was the first one found to include some (SMASS) L-class asteroids by Bus (1999).

As discussed above, we have only one polarimetric measurement of (2085) Henan and one measurement of the second largest member, (2354) Lavrov, the latter having been observed at a phase angle too small to draw any conclusion about its behaviour. The only one measurement of Henan, however, indi-
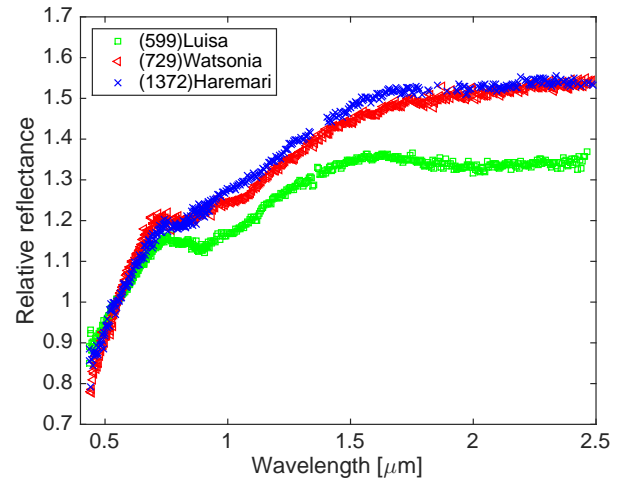
cates a very high probability of being a Barbarian.
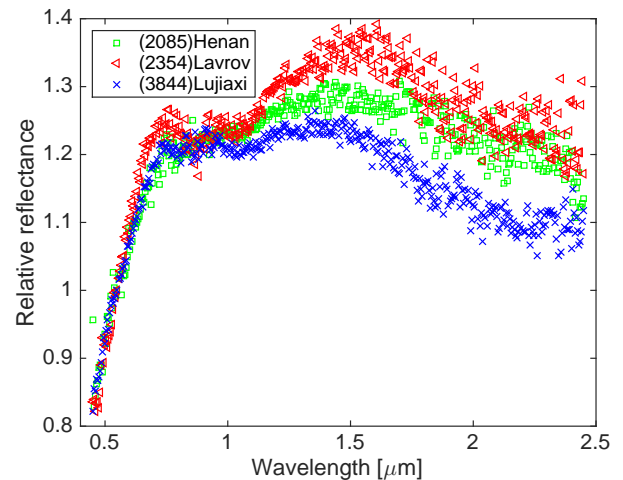
A few NIR spectra of Henan candidate members exist in the literature. Most of them are (DM) L-class and look similar, strengthening the possibility of a common origin. According to our modelling attempts, these objects are characterized by value of CAI ranging from 10 to 28 %, and display moderate value of space weathering. Fig. 19 shows the spectra of (2085) Henan, (2354) Lavrov, and (3844) Lujiaxi. A spectrum of (1858) Lobachevski is also available, however, this asteroid was classified as an S-type and possesses an albedo of 0.37. This make it probably an interloper inside the Henan family.

Some differences are noticed between the Henan and the Watsonia family. Henan family spectra exhibits a negative slope in the near-infrared region whereas members of the Watsonia family display positive slope. However, the visible spectral region shows identical behaviour.

20

5.6.3. The Tirela/Klumpkea family

The Tirela family was first identified by Nesvorný et al. (2005). It is located at the edge of the outer belt (proper semi-major axis $a_p = 3.12$ AU) and possesses high eccentricity and inclination ($e_p = 0.20$ and $i_p = 16.8°$). This family is characterized by high geometric albedo ($0.2 - 0.3$), whereas nearby asteroids in the same region have generally low albedo. This family was found to include (SMASS) L/Ld-class members by Mothé-Diniz and Nesvorný (2008). Milani et al. (2014) found also a family in this region, but they assigned a different membership and called it the Klumpkea family.

We observed (1040) Klumpkea in polarimetry, but only at low phase angles which cannot provide a diagnostic of Barbarian properties. In spectroscopy, five Tirela family members (8250), (15552), (19369), (26219), and (67255) were observed, but only in the NIR. However, for some of them, spectro-photometric data in the visible domain are available in the SDSS database. Their NIR spectra are characterized by strong 2 μm absorption band which leads to high abundance of CAIs. Only (19369) is lacking a strong 2 μm absorption band. This asteroid also possesses lower albedo than all other Tirela/Klumpkea family asteroid observed in this work. We suspect this asteroid to be an interloper inside this family. For the other ones, the spectral modeling provide CAIs abundance ranging from 13 to 23 % associated with almost no meteoritic component and high fraction of olivine.

6. Conclusions and perspectives

Our comprehensive analysis of the evidence coming from polarimetric and spectroscopic data allows us to draw some robust conclusions as well as some more tentative interpretation attempts based on current observational evidence.

The most robust result is the proven equivalence between the polarimetric Barbarian behaviour and the taxonomic classification as L-class objects according to the DeMeo et al. (2009) taxonomy. This correlation between polarimetric and spectroscopic behaviour had been already suggested in the past, we show in this work a very convincing observational proof of that.

Another important result is that we confirm preliminary conclusions by Sunshine et al. (2008a), and we find that the spectra of (DM) L-class objects can be successfully modelled using primitive materials, including primarily CAIs, MgO-rich olivine and the mineral compounds forming CV3s meteorite. We tried two CV3 meteorites in our Hapke model. We obtained better results when using the CV3 displaying CAIs with more FeO-rich spinels and showed some possible clue of aqueous alteration (Y-89751). We could also rule out the presence of large amounts of pyroxene. Our fits of available reflectance spectra were generally good, both in the NIR and the visible spectral regions.

An essential feature in our modelling exercises is that the presence of fluffy type A CAIs are needed to obtain acceptable fits of the reflectance spectra. We found evidence of a relation between the relative abundance of CAIs on the surface of these asteroids and the large polarimetric inversion angle which characterizes the Barbarian behaviour. Such a relation seems to be strengthened by the observed variation of the inversion angle of asteroid (234) Barbara as a function of wavelength. This variation can be interpreted as due to the wavelength-dependent variation of the refractive index of the spinel mineral.

Other possible explanations of the Barbarian behaviour, however, cannot be ruled out, including the possibility that Barbarians have surface regoliths formed by very thin particles, as suggested by Cellino et al. (2016a). Of course, different possible explanations are not necessarily mutually exclusive. Instead, the high abundance of fluffy type A CAI suggest that Barbarian asteroids could be extremely old and primitive.

The important role played by space weathering processes was also stressed by the results of our investigations. A tentative relation was found between the estimated abundance of nano phases iron believed to be characteristic outcomes of space weathering, and the extreme value of negative polarization $P_{\min}$.

Polarimetric and NIR reflectance spectra of a few members of dynamical families known to include L-class members were also obtained. We could confirm an L-classification for some of these family members. This is the first step of an investigation that deserves to be pursued making use of large telescopes. We plan also to extend our analysis in the future, by setting up laboratory activities, including polarimetric measurements of CAI material found in meteorite samples. These laboratory measurements will allow to definitely understand the polarimetric behaviour of CAIs and be able to provide more robust answers to the enigma represented by Barbarian asteroids.

Amelin, Y., Krot, A., Hutcheon, I., Ulyanov, A., 2002, Science, 297, 1678

Bagnulo, S., Cellino, A., Sterzik, M.F., 2015, MNRAS Lett., 446, L11

Bagnulo, S., Belskaya, I., Boehnhardt, H., Kolokolova, L., Muinonen, K.,Sterzik, M., Tozzi, G.-P., 2011, JQSRT, 112, 2059

Belskaya, I.N. et al., 2017, Icarus, 284, 30

Brož, M., Morbidelli, A., Bottke, W. F., Rozehnal, J., Vokrouhlický, D., Nesvorný, D., 2013, A&A, 551, A117

Brunetto, R., and Strazzulla, G., 2005, Icarus, 179, 265

Brunetto, R. et al., 2014, Icarus 237 278

Burbine, T., Gaffey, M., Bell, J., Meteoritic & Planetary Science, 1992, 27, 424

Burbine, T., Binzel, 2002, Icarus 159, 468

Compositional structure in the asteroid belt: Results of a spectroscopic survey. Ph.D. thesis, Massachusetts Institute of Technology, 1999.

Bus S., Binzel R., 2002, Icarus, 158, 146

Bus, S. J., Ed., IRTF Near-IR Spectroscopy of Asteroids V1.0. EAR-A-I0046-4-IRTFSPEC-V1.0. NASA Planetary Data System, 2009.

Binzel, R. P., Harris, A. W., Bus, S. J., and Burbine, T. H., 1992, Icarus 151, 139

Binzel, R. P., et al. 2004, Icarus 170, 259

Bland, P.A., Cressey, G., Menzies, O.N., 2004,. Meteorit. Planet. Sci, 39, 3.

Carry, B., Solano, E., Eggl, S., DeMeo, F., 2016, Icarus, 268, 340

Cellino, A., Belskaya, I. N., Bendjoya, Ph., di Martino, M., Gil-Hutton, R., Muinonen, K. and Tedesco, E. F. 2006, Icarus, 180, 565

Cellino, A., Delbò, M., Bendjoya, Ph., Tedesco, E., Icarus, 2010, 209, 556

Cellino, A., Bagnulo, S., Tanga, P., Novaković, B., Delbo, M., 2014a, MNRAS 2014a, 439, 75

Cellino, A., Bagnulo, S., Gil-Hutton, R., Tanga, P., Cañada-Addandi, M., Tedesco, E. F., 2015a, MNRAS, 451, 3473

Cellino, A., Bagnulo, S., Gil-Hutton, R., Tanga, P., Caảda-assandri, M., Tedesco, E. F., 2016a, MNRAS, 455, 2091

Cellino, A., Ammannito, E., Magni, G., Gil-Hutton, R., Tedesco, E.F., Belskaya, I.N., De Sanctis, M.C., Schroeder, S., Preusker, F., Manara, A. 2016b, MNRAS, 456, 248

Chapman, C., 1996, Meteoritic & Planetary Science, 31, 699

Cloutis E.A., Hudon, P., Hiroi, T., Gaffey M.J., Mann, P., Bell, J.F., 2012, Icarus, 221, 328

Coradini et al., 2011, Science, 334, 492

Cushing, M., Vacca, W., Rayner, J., 2004, Publications of the Astronomical Society of the Pacific, 116, 818

DeMeo, F., Binzel, R., Slivan, S and Bus, S, 2009, Icarus, 202, 160

Devogèle M. et al. MNRAS, 2017a, 465, 4335

Devogèle M. et al., 2017b, Accepted to A&A

Dollfus, A., Wolff, M., Geake, J. E., Dougherty, L. M., Lupishko, D. F., 1989, in Asteroid II, University of Arizona Press; Tucson, AZ (USA), 594

Farinella, P.,Davis, D., Cellino, A., Zappala, V. 1992, A&A, 257, 329

Gaffey, M.J., et al., 1993, Icarus, 106, 573

Gil-Hutton, R., Mesa, V., Cellino, A., Bendjoya, P., Peñaloza L., Lovos F., 2008, A&A, 482, 309

Gil-Hutton, R. and Cañada-Assandri, M. , 2011, A&A, 529, A86

Gil-Hutton, R., Cellino, A., Bendjoya, P., 2014, A&A, 569, A122

Gulkis et al., 2012, Planetary and Space Science, 66, 31

Gundlach, B., and Blum, J., 2013, Icarus, 223, 479

Gomes, R., Levison, H.F., Tsiganis, K., Morbidelli, A., 2005, Nature, 435, 466

Grimm, R. E., McSween Jr, H. Y., 1989, Icarus, 82, 244.

Gyollai, I., Nagy, Sz., Bérczi, Sz., Gucsik, A., 2011. Lunar Planet. Sci. 42. Abstract #1039.

Hanus, J., Durech, J., Oszkiewicz, D.A.,Behrend, R., et al., 2016, A&A, 586, A108.

Hanus, J., Durech, J., Broz, M., Marciniak, A., et al., 2013, A&A, 551, A67.

Hapke B., 1981, Journal of Geophysical Reseach, 86, 3039

Hapke B., 1984, Icarus, 59, 41

Hapke B., 1986, Icarus, 67, 264

Hapke B., 1993, Theory of reflectance and emittance spectroscopy., Cambridge : Cambridge University Press.

Hapke B., 2001, Journal of Geophysical Research, 106, 10039

Henning, Th., Begemann, B., Mutschke, H., Dorschner, J., 1995, Astron. Astrophys. Suppl. Ser. 112 (1995), 143-149

Hosseini, S., 2008, Phys. Stat. Sol., 245, 2800

Ivezić, Ž., et al.,2002, Astron. J., 124, 2943

Jockers, K., et al., 2000, Kinematika i Fizika Nebesnykh Tel Supplement, 3, 13

Lantz, C., Brunetto, R., Barucci, M.A., Fornasier, S., Baklouti, D., Bourcois, J., Godard, M., 2017, Icarus, 285, 43

Lord S., 1992, A New Software Tool for Computing Earths Atmospheric Transmissions of Near- and Far-Infrared Radiation, NASA Technical Memoir 103957 (Moffett Field, CA: NASA Ames Research Center)

Lucey, P., 1998, Journal of geophysical research, 103, 1703

Mainzer, A.K. et al. , 2016, NEOWISE Diameters and Albedos V1.0. EAR-A-COMPIL-5-NEOWISEDIAM-V1.0. NASA Planetary Data System, 2016.

Masiero, J. and Cellino, A., 2009, Icarus, 199, 333

Masiero, J. et al., ApJ, 2011, 741, 68

Masiero J., Mainzer, A., Bauer, J., Grav, T., Nugent, C., Stevenson, R., 2013, ApJ, 777, 7

Masiero, J.R., DeMeo, F.E., Kasuga, T., Parker, A.H., 2015, in "Asteroids IV" (Michel, P., DeMeo, F.E., Bottke, W.F., Eds), p.323, University of Arizona Press, Tucson, AZ, USA.

Mason, B, Geochimica et Cosmochimica Acta, 2013, 27, 1011

Mothé-Diniz, T., and Nesvorný, D., 2008, A&A 492, 593

Milani, A., Cellino A., KneĂevi, Z., Novakovi, B., Spoto, F., Paolicchi, P., 2014, Icarus, 46, 239

Muinonen, K., Piironen, J., Shkuratov, Y. G., Ovcharenko, A. A., Clark, B.E. et al., 2002, Asteroid photometric and polarimetric phase affects In Asteroid III (W.F. Bottke Jr. et al., eds.), 123

Muinonen, K., Penttila, A., Cellino, A., Belskaya, I. N., Delbo, M., Levasseur-Regourd, A.-C., Tedesco, E.F., 2009, Meteoritics and Planet. Sci., 44, 1937

Murakami, T, Ikeda., Y., 1994, Meteoritics, 29, 397

Mustard, J., Pieters, C., 1989, Journal of Geophysical Research, 94, 13619

Nash, D.B. and Conel, J.E., 1974 Journal of Geophysical Research 79, 1615

Nesvorný, D., Broz, M., Carruba, V., 2015 in Asteroids IV

Nesvorný, D., Jedicke, R., Whiteley, R. J., Ivezic, Z. 2005, Icarus, 173, 132

Novaković, N., Cellino, A., Knežević, Z., 2011, Icarus, 216

ORourke, L., 2012, Planetary and Space Science, 66, 192

Palme, H., Spettel, B., Ikeda, Y., 1993., Meteoritics 28, 417 (abstract).

Penttilä, A., Lumme, K., Hadamcik, E., Levasseur-Regourd, A.-C., 2005, Å, 432, 1081

Pernechele, C., Abe, L., Bendjoya, Ph., Cellino, A., Massone, G., Tanga, P., 2012, Proceedings of the SPIE, 8446, 84462H

Pieters, C. M., Fischer, E., Rode, O., Basu, A., 1993, Geophys. Res., 98, 20817

Rayner et al., 2003, Publications of the Astronomical Society of the Pacific, 115, 805

Rivkin, A. S., Trilling, D. E., Lebofsky, L. A. Bull. Am. Astron. Soc. 30, 1023 (1998).

Ryan, E.L., Woodward, C.E., 2010, The Astronomical Journal, 140, 934

Shkuratov, Y. G. et al., 1994, EM&P, 65, 201

Sierks, H., et al., 2011, Science, 334, 487

Spoto, F., Milani, A., Knežević, Z., 2015, Icarus, 257, 275

Sunshine et al., 2007, Lunar and Planetary Institute Science Conference Abstract, 1613

Sunshine et al., 2008, Science, 320, 514

Sunshine et al., 2008, American Astronomical Society, DPS meeting #40, id.60.07; Bulletin of the American Astronomical Society, 40, 509

Shui, X., Binzel, R., Burbine, T., Bus, S., 2009, 115, 1

Tanga, P., et al., 2015, MNRAS, 448, 3382

Tedesco, E.F, 1989, in Asteroid II, 1090

Tedesco, E.F, Desert, F-X., 1989, The Astronomical Journal, 123, 2070

Tholen, D.J. 1984, "Asteroid Taxonomy from Cluster Analysis of Photometry". PhD thesis, University of Arizona.

Tholen, D.J., and Barucci, M.A., 1989, in "Asteroids II" (Binzel, R.P., Gehrels, T. and Shapley Matthews, M., Eds), p.298, University of Arizona Press, Tucson, AZ, USA.

Usui, F. et al., 2012, The Astrophysical Journal, 762, 1

Xu, S., Binzel, R., Burbine, T., Bus, S., 1995, Icarus, 115, 1

Zellner, B., Tholen, D.J., and Tedesco, E.F., Eight Color Asteroid Survey. EAR-A-2CP-3-RDR-ECAS-V4.0. NASA Planetary Data System, 2009.

Zubko, E., Videen, G., Shkuratov, Y., 2015, Journal of Quantitative Spectroscopy & Radiative Transfer

Zubko, E., Videen, G., Shkuratov, Y., Muñoz, O., Y., 2016, 47th Lunar and Planetary Science Conference, held March 21-25, 2016 at The Woodlands, Texas. LPI Contribution No. 1903, p.2111

Zappalà, V., Cellino, A., Dell'Oro, A., Paolicchi, P, 2002, in "Asteroids III" (Bottke, W.F., Cellino, A., Paolicchi, P., Binzel, R.P., Eds), p.613, University of Arizona Press, Tucson, AZ, USA.

Appendix A. Spectra observed in this work

Appendix B. Results of spectra fitting presented in this work

Appendix C. Polarimetric observation presented in this work

Object Number	Date	Phase [Deg]	P_r [%]	Observatory
12	04/02/2016	9.83	-0.889 ± 0.040	Calern
122	20/05/2015	3.07	-0.475 ± 0.022	Calern
122	22/05/2015	3.45	-0.553 ± 0.032	Calern
122	04/07/2016	7.24	-0.795 ± 0.032	Calern
122	26/07/2016	0.61	-0.023 ± 0.032	Calern
122	18/08/2016	7.79	-0.635 ± 0.130	Calern
172	10/10/2015	23.17	-0.699 ± 0.046	Calern
172	09/12/2015	12.00	-1.345 ± 0.040	Calern
234	25/02/2015	16.95	-1.543 ± 0.070	Calern
234	22/05/2015	17.38	-1.430 ± 0.026	Calern
234	19/07/2016	33.54	0.620 ± 0.046	Calern
234	04/12/2016	18.34	-1.494 ± 0.090	Calern
236	22/02/2015	11.50	-1.314 ± 0.040	Calern
236	30/03/2015	0.41	0.032 ± 0.027	Calern
236	21/05/2015	15.26	-1.240 ± 0.040	Calern
236	07/06/2016	5.02	-0.873 ± 0.064	Calern
236	05/07/2016	9.98	-1.085 ± 0.101	Calern
236	17/07/2016	13.93	-1.302 ± 0.069	Calern
236	26/07/2016	16.52	-1.238 ± 0.065	Calern
236	28/07/2016	17.05	-1.451 ± 0.079	Calern
387	10/10/2015	16.47	-1.374 ± 0.039	Calern
387	09/12/2015	12.97	-1.532 ± 0.040	Calern
387	10/04/2016	17.74	-1.430 ± 0.060	Calern
387	13/04/2016	17.80	-1.540 ± 0.060	Calern
387	01/12/2016	17.76	-1.240 ± 0.050	Calern
402	10/10/2015	17.35	-1.743 ± 0.057	Calern
402	14/10/2015	18.05	-1.698 ± 0.068	Calern
402	10/12/2015	19.36	-1.502 ± 0.106	Calern
402	01/12/2016	6.78	-1.060 ± 0.036	Calern
402	07/12/2016	7.45	-1.163 ± 0.041	Calern
402	09/12/2016	8.17	-1.458 ± 0.061	Calern
402	12/12/2016	8.99	-1.340 ± 0.082	Calern
402	27/12/2016	14.07	-1.714 ± 0.047	Calern
402	28/12/2016	14.42	-1.804 ± 0.041	Calern
402	03/01/2017	16.35	-1.795 ± 0.032	Calern
402	07/01/2017	17.28	-1.985 ± 0.091	Calern
402	16/01/2017	19.90	-1.580 ± 0.039	Calern
402	17/01/2017	20.15	-1.391 ± 0.052	Calern
402	24/01/2017	21.58	-1.412 ± 0.057	Calern
458	10/05/2016	16.15	-1.854 ± 0.080	Calern
460	06/08/2016	3.68	-1.435 ± 0.058	Calern
460	14/08/2016	3.19	-1.203 ± 0.074	Calern
460	21/08/2016	5.51	-1.454 ± 0.110	Calern
478	18/07/2015	7.80	-0.732 ± 0.099	Calern
478	21/07/2015	8.60	-0.683 ± 0.039	Calern
478	29/09/2015	17.82	-0.100 ± 0.100	Calern
478	29/07/2016	14.68	-0.622 ± 0.063	Calern
599	10/04/2016	10.09	-1.510 ± 0.100	Calern

Table C.5: Summary of our polarimetric measurements. The first column corresponds to the number of the observed asteroid. The second indicates the date of observation. The third one corresponds to the phase angle (angle between the sun-asteroid-observer). P_r is the polarization degree. Finally the Observatory column gives the observatory in which the data were acquired.
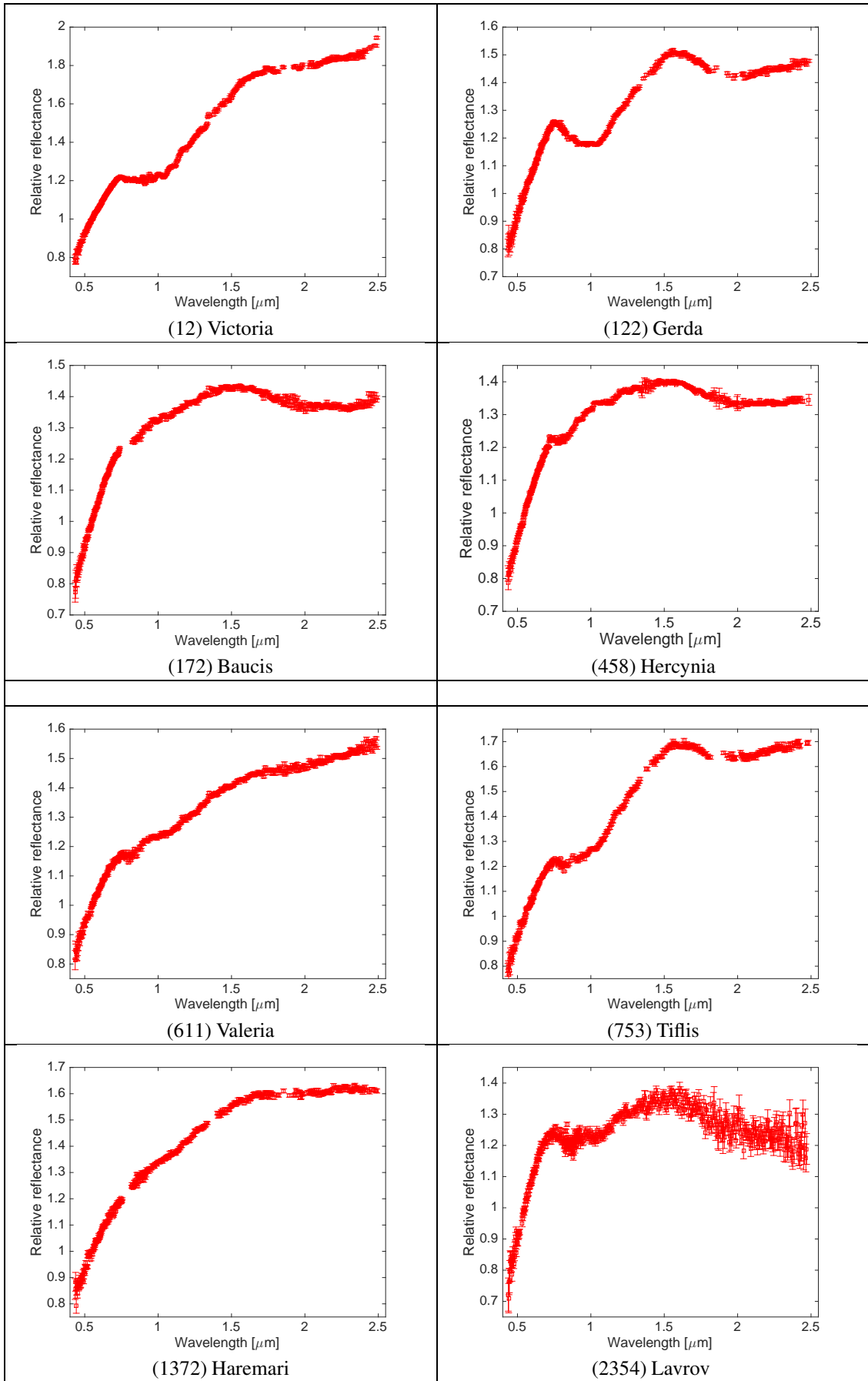
23

(12) Victoria

(122) Gerda

(172) Baucis

(458) Hercynia

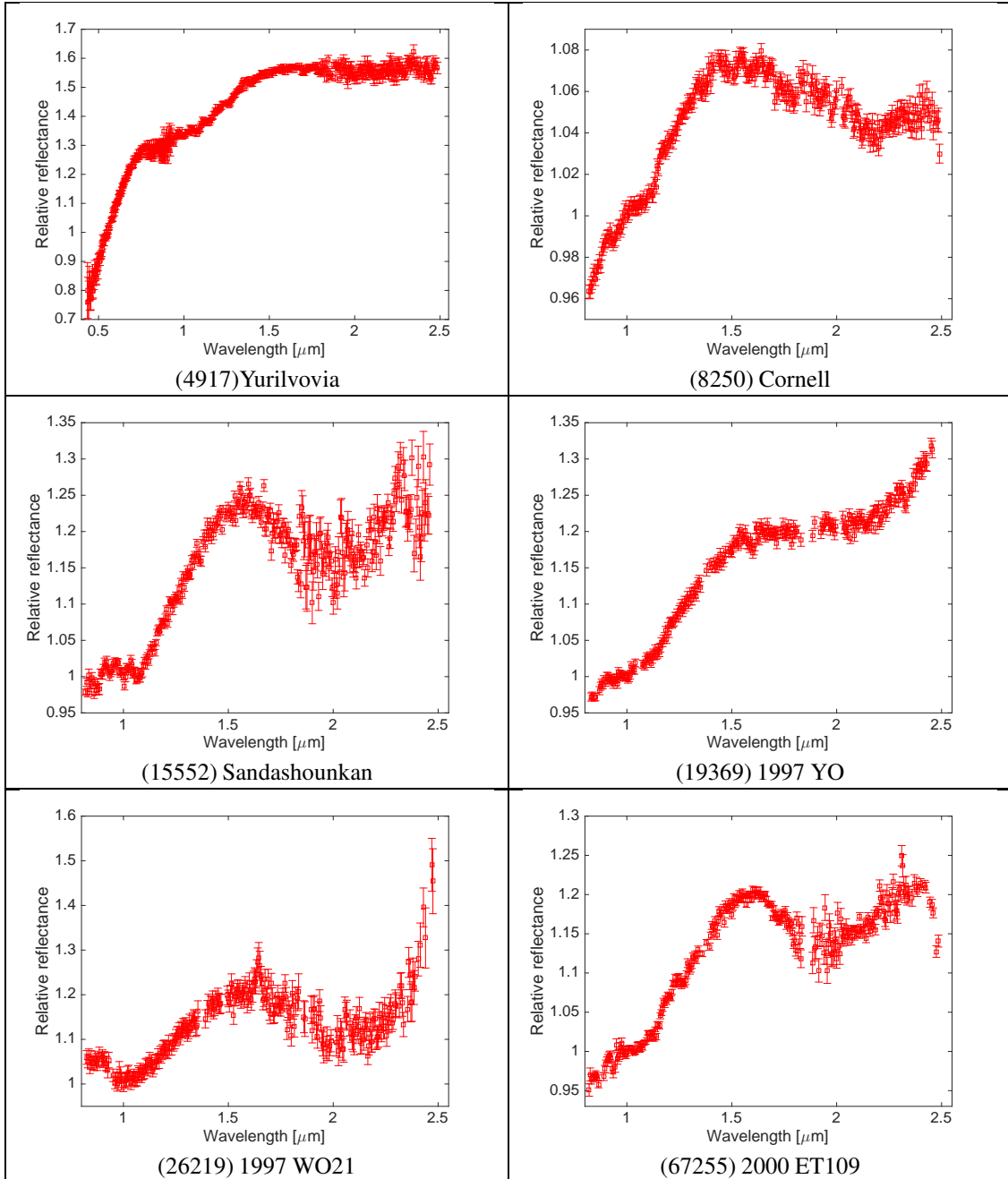(611) Valeria

(753) Tiflis

(1372) Haremari

(2354) Lavrov

Figure A.20: Spectra obtained during the two IRTF runs.

24

Figure A.20: Spectra obtained during the two IRTF runs.

Figure B.21: Spectra obtained during the two IRTF runs.

(599) Luisa
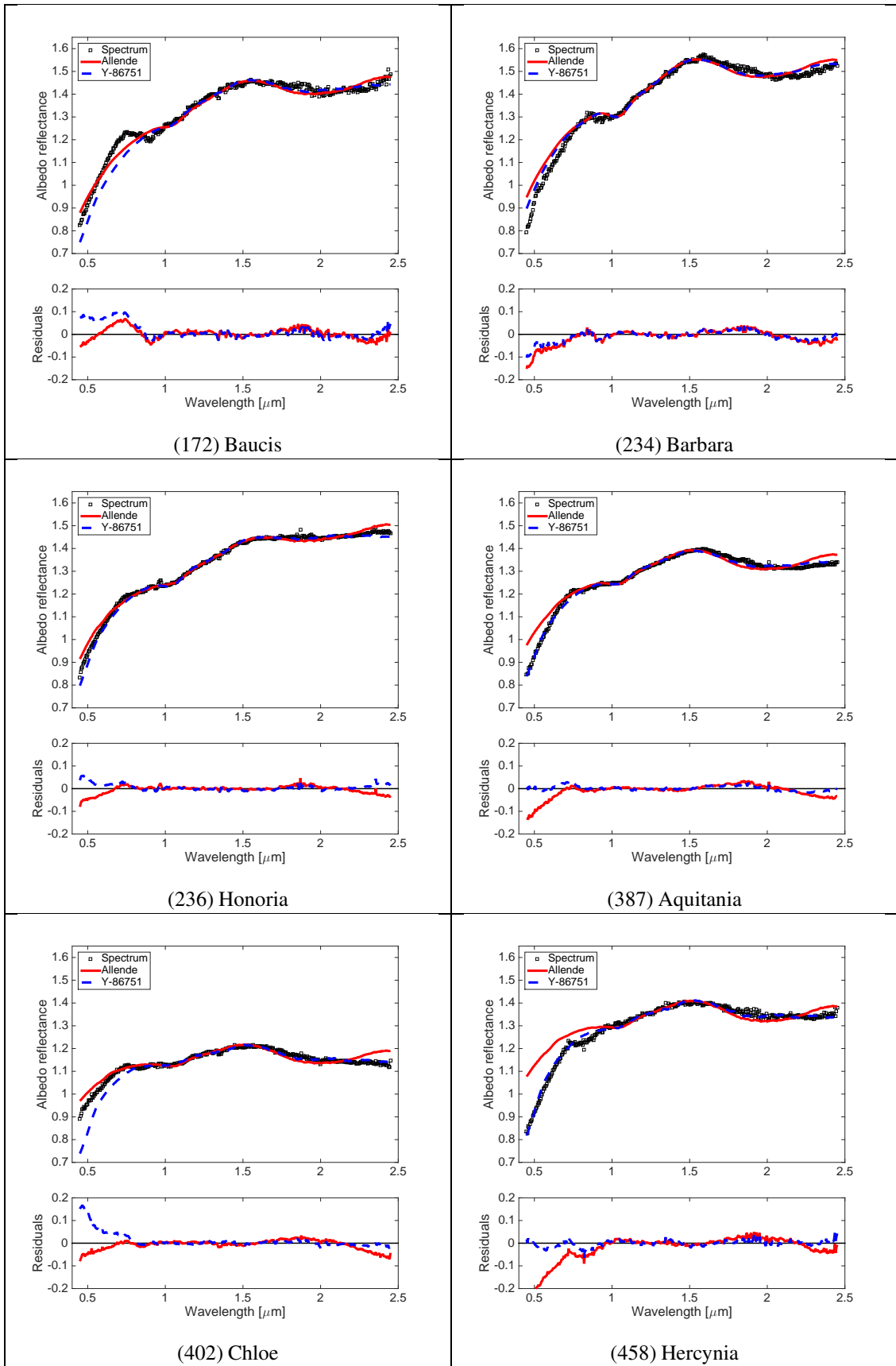
(611) Valeria

(673) Edda

(679) Pax

(729) Watsonia

(824) Anastasia

Figure B.21: continued

(980) Anacostia

(1372) Haremari

(2085) Henan

(2354) Lavrov

(2448) Sholokhov

(2732) Witt

Figure B.21: continued

(3734) Waland

(3844) Lujiaxi

(4737) Kiladze

(5840) Raybrown

(7763) Crabeels

(8250) Cornell
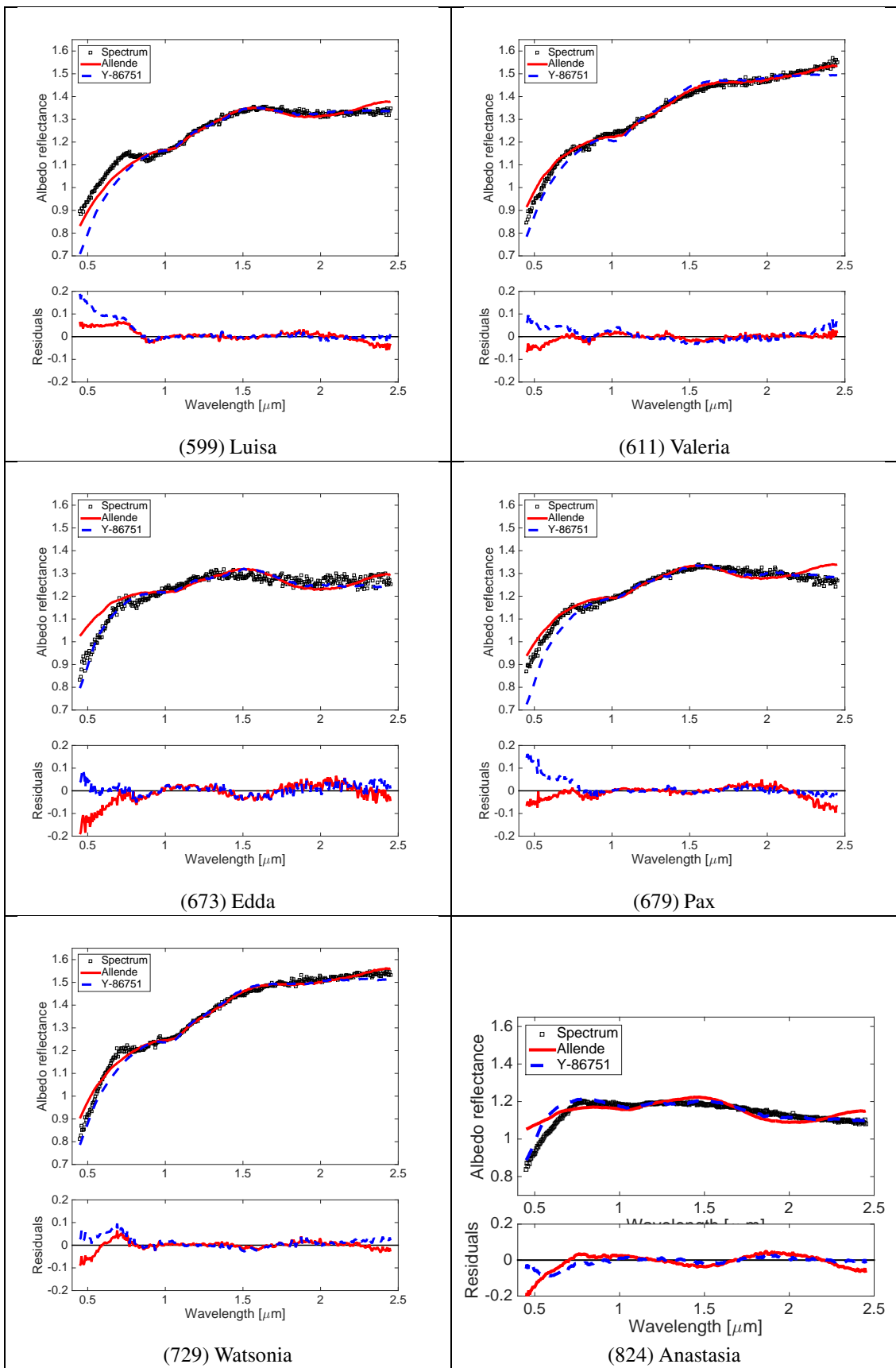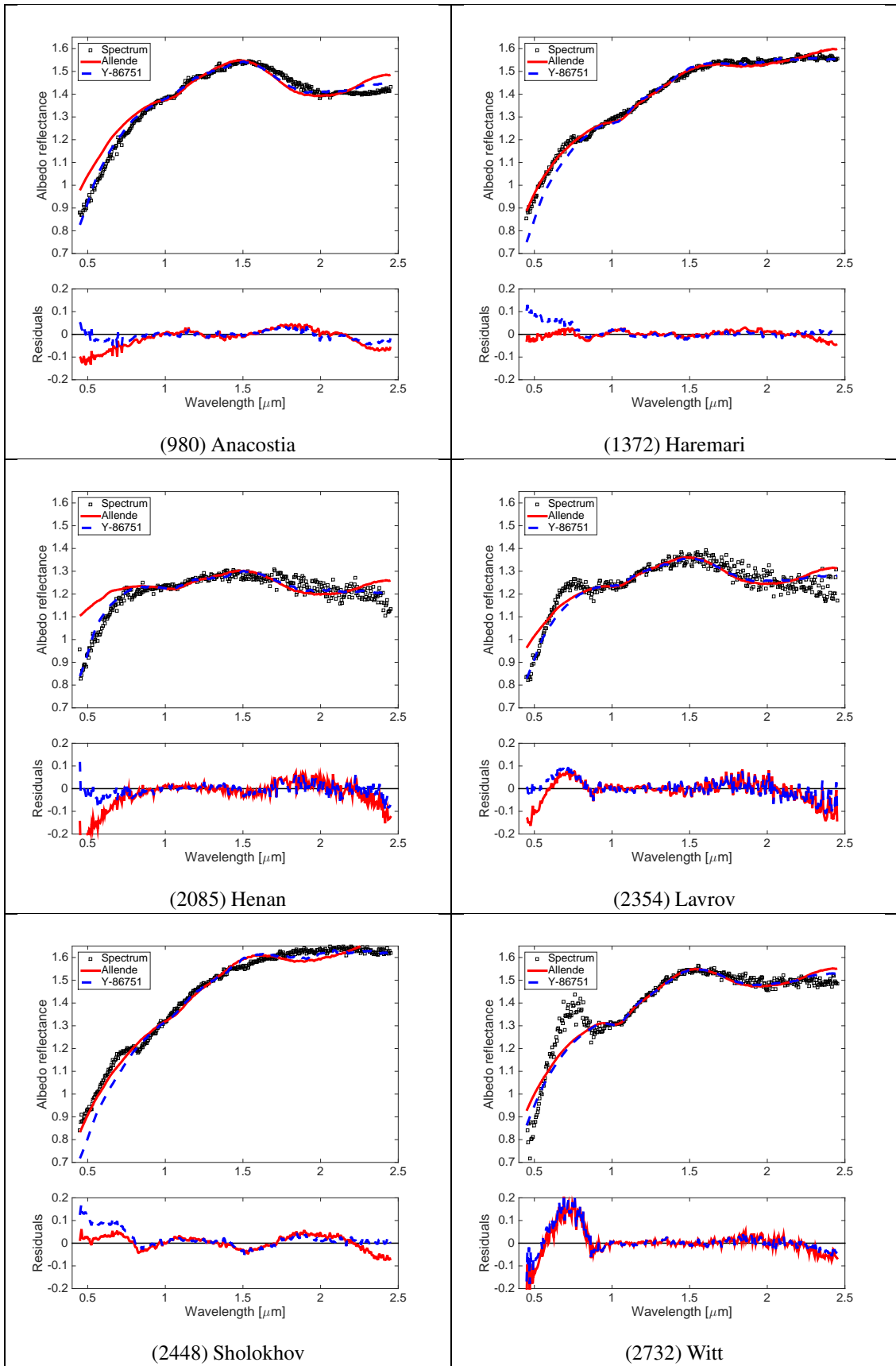
Figure B.21: continued
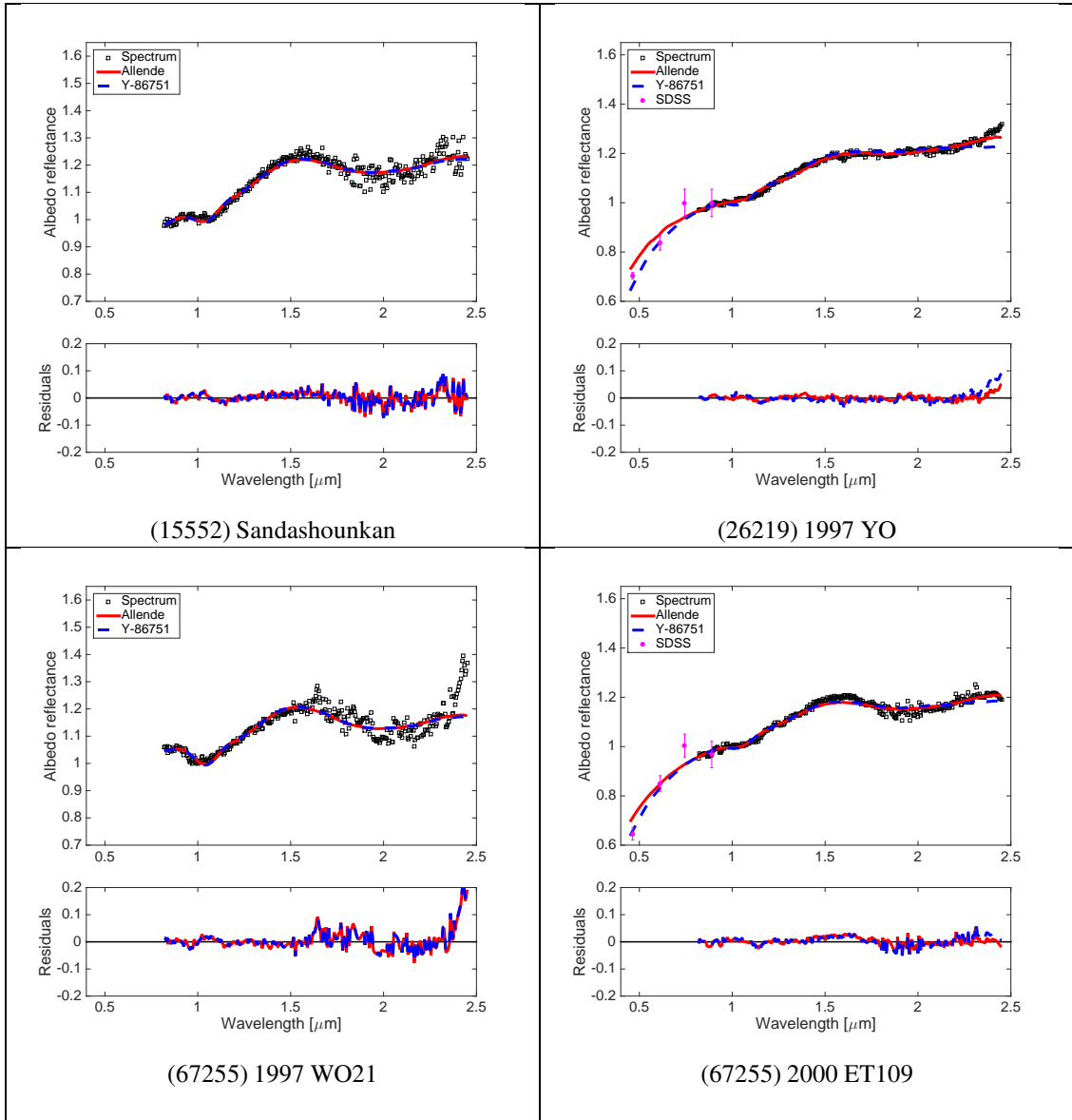
Figure B.21: continued

Object Number	Date	Phase [Deg]	P_r [%]	Observatory
606	10/12/2015	19.80	−1.130 ± 0.230	Calern
606	11/12/2015	19.60	−1.299 ± 0.114	Calern
611	20/12/2014	20.28	−0.920 ± 0.040	Rozhen
611	11/12/2015	19.28	−0.885 ± 0.057	Calern
642	10/10/2015	4.11	−0.950 ± 0.042	Calern
642	01/12/2016	8.42	−1.725 ± 0.070	Calern
642	07/12/2016	6.55	−1.328 ± 0.090	Calern
642	12/12/2016	4.98	−1.183 ± 0.094	Calern
642	03/01/2017	7.50	−1.556 ± 0.090	Calern
642	06/01/2017	8.49	−1.572 ± 0.115	Calern
679	13/07/2015	3.72	−0.595 ± 0.036	Calern
679	01/12/2016	22.27	−0.892 ± 0.044	Calern
679	09/12/2016	20.39	−1.272 ± 0.061	Calern
679	21/12/2016	17.01	−1.494 ± 0.061	Calern
679	27/12/2016	14.94	−1.625 ± 0.052	Calern
679	28/12/2016	14.57	−1.656 ± 0.038	Calern
679	16/01/2017	7.26	−1.158 ± 0.025	Calern
679	18/01/2017	6.52	−1.246 ± 0.051	Calern
729	11/12/2015	18.10	−1.334 ± 0.066	Calern
729	01/12/2016	13.86	−1.196 ± 0.055	Calern
729	04/12/2016	11.14	−1.040 ± 0.134	Calern
729	05/12/2016	10.82	−1.240 ± 0.066	Calern
729	06/12/2016	10.50	−1.171 ± 0.062	Calern
729	07/12/2016	10.18	−1.177 ± 0.060	Calern
729	08/12/2016	9.86	−1.183 ± 0.122	Calern
729	10/12/2016	9.21	−0.882 ± 0.133	Calern
729	12/12/2016	8.56	−0.843 ± 0.100	Calern
729	13/12/2016	8.22	−1.057 ± 0.050	Calern
729	23/12/2016	5.17	−0.891 ± 0.047	Calern
729	27/12/2016	4.35	−0.644 ± 0.040	Calern
729	28/12/2016	4.21	−0.705 ± 0.046	Calern
729	03/01/2017	4.37	−0.662 ± 0.031	Calern
729	06/01/2017	4.96	−0.796 ± 0.103	Calern
729	16/01/2017	7.99	−1.108 ± 0.050	Calern
729	19/01/2017	8.72	−1.104 ± 0.064	Calern
753	11/12/2015	23.96	−0.123 ± 0.100	Calern
824	13/07/2015	3.35	−0.795 ± 0.051	Calern
824	15/07/2015	3.74	−0.924 ± 0.051	Calern
824	04/12/2016	11.41	−2.154 ± 0.119	Calern
824	13/12/2016	13.76	−2.589 ± 0.212	Calern
824	09/01/2017	18.11	−1.714 ± 0.176	Calern
908	08/12/2015	22.01	−0.381 ± 0.033	Calern
908	04/12/2016	25.36	0.640 ± 0.166	Calern
980	04/07/2016	3.02	−0.607 ± 0.033	Calern
980	22/07/2016	6.01	−0.771 ± 0.053	Calern
980	26/07/2016	7.98	−1.032 ± 0.076	Calern
980	05/08/2016	12.48	−1.320 ± 0.064	Calern
980	10/08/2016	14.54	−1.175 ± 0.107	Calern
980	02/12/2016	22.30	−0.775 ± 0.041	Calern
1040	06/08/2016	4.14	−0.121 ± 0.088	Calern
1040	12/08/2016	4.71	−0.388 ± 0.106	Calern
1040	22/08/2016	6.94	−1.042 ± 0.119	Calern

Table C.5: continued

Object Number	Date	Phase [Deg]	P_r [%]	Observatory
1284	10/10/2015	9.23	−1.926 ± 0.054	Calern
1284	09/12/2015	25.20	−0.190 ± 0.040	Calern
1284	09/12/2016	22.95	−0.531 ± 0.082	Calern
1284	10/12/2016	22.89	−0.548 ± 0.258	Calern
1332	20/12/2014	16.64	−0.630 ± 0.170	Rozhen
1332	10/04/2016	8.90	−2.100 ± 0.300	Calern
1372	26/02/2015	19.96	−0.911 ± 0.124	Calern
1406	04/12/2016	11.06	−0.441 ± 0.101	Calern
1702	22/05/2015	7.39	−1.076 ± 0.650	Calern
1702	02/08/2016	12.08	−1.007 ± 0.108	Calern
1702	22/08/2016	5.75	−0.718 ± 0.068	Calern
2085	19/12/2014	15.82	−1.920 ± 0.090	Rozhen
2354	11/12/2015	3.54	−0.653 ± 0.069	Calern
2448	04/12/2016	20.27	0.055 ± 0.129	Calern
2448	21/12/2016	17.35	−0.643 ± 0.119	Calern
2732	06/12/2016	8.86	−0.772 ± 0.330	Calern
3269	05/12/2016	12.48	−0.919 ± 0.275	Calern

Table C.5: continued